Statistical Analyses of Satellite Cloud Object Data from CERES. Part III: Comparison with Cloud-resolving Model Simulations of Tropical Convective Clouds

Yali Luo[1], Kuan-Man Xu[2], Bruce. A. Wielicki[2]

Takmeng Wong[2], and Zachary A. Eitzen[3]

[1]National Institute of Aerospace, Hampton, VA
[2]NASA Langley Research Center, Hampton, VA
[3]Science Applications International Corporation, Hampton, VA

Submitted to
Journal of Atmospheric Sciences

March 1, 2006

Revised June 26, 2006

Corresponding author address:
Dr. Yali Luo
National Institute of Aerospace
100 Exploration Way
Hampton, VA 23666-6147
e-mail: yali@nianet.org

Abstract

The present study evaluates the ability of a cloud-resolving model (CRM) to simulate the physical properties of tropical deep convective cloud objects identified from a Clouds and the Earth's Radiant Energy System (CERES) data product. The emphasis of this study is the comparisons among the small-, medium- and large-size categories of cloud objects observed during March 1998 and between the large-size categories of cloud objects observed during March 1998 (strong El Niño) and March 2000 (weak La Niña). Results from the CRM simulations are analyzed in a way that is consistent with the CERES retrieval algorithm and they are averaged to match the scale of the CERES satellite footprints. Cloud physical properties are analyzed in terms of their summary histograms for each category.

It is found that there is a general agreement in the overall shapes of all cloud physical properties between the simulated and observed distributions. Each cloud physical property produced by the CRM also exhibits different degrees of disagreement with observations over different ranges of the property. The simulated cloud tops are generally too high and cloud top temperatures are too low except for the large-size category of March 1998. The probability densities of the simulated top-of-the-atmosphere (TOA) albedos for all four categories are underestimated for high albedos, while those of cloud optical depth are overestimated at its lowest bin. These disagreements are mainly related to uncertainties in the cloud microphysics parameterization and inputs such as cloud ice effective size to the radiation calculation.

Summary histograms of cloud optical depth and TOA albedo from the CRM simulations of the large-size category of cloud objects do not differ significantly between the March 1998 and 2000 periods, consistent with the CERES observations. However, the CRM is unable to reproduce the significant differences in the observed cloud top height while it overestimates the differences in the observed outgoing longwave radiation and cloud top temperature between the two periods. Comparisons between the CRM results and the observations for most parameters in March 1998 consistently show that both the simulations and observations have larger differences between the large- and small-size categories than between the large- and medium-size, or between the

medium- and small-size categories. However, the simulated cloud properties do not change as much with size as observed. These disagreements are likely related to the spatial averaging of the forcing data and the mismatch in time and in space between the numerical weather prediction model from which the forcing data are produced and the CERES observed cloud systems.

1. Introduction

It is well known that clouds play a major role in modulating the Earth's radiant energy balance, and hence influence climate, through their effects on both incoming shortwave and outgoing longwave radiation. Global climate models (GCMs) are a major tool for climate study. In GCMs, physical processes are represented within arrays of grid boxes that have much larger spatial scales than those of clouds, and so clouds have to be represented statistically in terms of the resolvable-scale variables. This is also known as the cloud parameterization problem (Arakawa 2004). The underlying assumptions used in cloud parameterizations should be based upon observed cloud characteristics, but simplifications have to be made due to limited understanding of the problem. Despite numerous efforts to evaluate and improve cloud parameterizations, the progress in the cloud parameterization problem has been slow (IPCC 2001; Randall et al. 2003).

A recently proposed multiscale modeling framework (MMF) approach has the potential to further advance climate modeling by replacing most of the traditional physical parameterizations in each grid cell of a GCM with a high-resolution cloud-system resolving model (CRM; Grabowski 2001; Khairoutdinov and Randall 2001). This approach allows for an explicit simulation of many cloud processes, including convection, overlapping clouds in both the radiative and microphysical senses, and convectively generated gravity waves, as pointed out by Randall et al. (2003). Preliminary tests of the MMF approach have indicated that a GCM with an embedded CRM can produce the Madden-Julian Oscillation as well as higher-frequency tropical waves in a much more realistic manner than a GCM with a traditional cloud parameterization (Grabowski 2003; Randall et al. 2003). However, the embedded CRM must be evaluated for a variety of cloud system types using observational data to narrow down the uncertainties associated with its parameterizations of cloud microphysics, radiative transfer, and turbulence.

Previously, CRMs have been evaluated statistically against a limited number of field experiment data. For example, Xu and Randall (1996), Grabowski et al. (1996), Tao et al. (2003), and Johnson et al. (2004) performed 2-D CRM simulations of tropical convective systems observed in several geographic locations. Xu and Randall (2000) examined the performance of a

CRM in simulating midlatitude convection using the Department of Energy Atmospheric Radiation Measurement (ARM) program (Stokes and Schwartz 1994; Ackerman and Stokes 2003) intensive operational period (IOP) data. Xu et al. (2002, 2005) presented intercomparison studies of midlatitude convection and frontal clouds simulated by several CRMs using different ARM IOP data. Luo et al. (2003) compared cirrus cloud properties simulated by a CRM with cloud radar observations obtained by Mace et al. (1998) at the ARM Southern Great Plains site. However, this type of evaluation of CRMs is restricted to a limited number of cloud regimes in a few geographic locations where the field experiments were conducted.

Xu et al. (2005; hereafter Part I) recently proposed a "cloud object" methodology to analyze statistical properties of cloud systems from Earth Observing System (EOS) satellites in order to more rigorously validate model simulations. This approach identifies a cloud object as a contiguous patch of the Earth composed of satellite footprints within a single dominant cloud-system type. The shape and size of each cloud object are determined by the satellite footprint data and by the selection criteria based upon cloud physical properties for a given cloud-system type. No fixed region of the Earth is used in this new methodology. It is therefore *not* an Eulerian approach, in contrast to monthly-averaged satellite observations. This approach advances cloud model/parameterization evaluation by using large, statistically robust ensembles of matched atmospheric states and satellite cloud object data, with an emphasis on evaluating the statistical distributions of fine-scale characteristics of cloud objects.

The cloud object data product described in Part I of this series of study includes four major cloud types, i.e., tropical deep convection and boundary-layer cumulus, stratocumulus and stratus clouds. This data product can be expanded to include other cloud types such as thin anvil clouds and polar clouds with the availability of CloudSat (Stephens et al. 2002) and Cloud-Aerosol Lidar and Infrared Pathfinder Satellite Observations (CALIPSO; Winker et al. 2003) satellite data. The statistical distributions of cloud physical properties are contrasted between the strong 1997/1998 El Niño in March 1998 and the weak La Niña in March 2000 in Part I. For tropical deep convective cloud objects, most of these properties were similar except for some of the cloud macrophys-

ical properties. Part II (Xu et al. 2006) examined characteristics of tropical deep convective cloud objects observed over the tropical Pacific during January-August 1998. It was found that statistical distributions of cloud physical properties are significantly different among three size categories of cloud objects with equivalent diameters of 100-150 km (small-size category), 150-300 km (medium-size category) and > 300 km (large-size category), respectively, except for the distributions of ice particle size.

The main objective of the present study is to evaluate the performance of a CRM to be used in the MMF approach for reproducing the observed characteristics of tropical deep convective cloud objects presented in Parts I and II of this series of the study. Specifically, can the CRM capture the differences and similarities in the observed statistical characteristics between the March 1998 and March 2000 periods? Can the CRM produce the different statistical characteristics among the three size categories of cloud objects observed in March 1998? The present study adopts an approach similar to that presented in Eitzen and Xu (2005; EX05 hereafter) except for including simulations of more size categories and the March 2000 period. Another difference is that the CRM used in this study is currently being implemented in an MMF, but that in EX05 is not. In addition, there are also some methodological differences used in comparing the CRM simulations with satellite data in these two studies, which will be described in more detail later.

Section 2 describes the observational data. The CRM, the design of CRM simulations, and the methodology to analyze the CRM results are presented in Section 3. Simulated cloud physical properties for the large-size categories of cloud objects are compared with the observational data in Section 4. Section 5 contains comparisons among the three size categories of cloud objects. Sensitivities of the CRM results to analysis methods and cloud ice effective size formulations are presented in Section 6. Summary and discussion are given in Section 7 and Section 8, respectively.

2. Description of observational data

The observational data used in this study are extracted from the Clouds and the Earth's Radiant Energy System (CERES; Wielicki et al. 1996) Single Scanner Footprint (SSF) data product deducted from the Tropical Rainfall Measuring Mission (TRMM) satellite measurements. The CERES SSF dataset contains cloud properties and broadband radiation measurement for each CERES/TRMM satellite footprint (Wielicki et al. 1998). The average size of the CERES/TRMM footprint is approximately 100 km^2. The cloud properties are determined from measured radiances at individual imager pixels (2 km resolution) using state-of-the-art methods (Minnis et al. 1997). The imager cloud properties are convolved and averaged into the larger-size CERES footprints (Green and Wielicki 1997). These footprint measurements were used in Part I to identify four types of distinct cloud objects. These cloud object data are available from the cloud object data website at http://cloud-object.larc.nasa.gov/. This study will concentrate only on simulating the tropical deep convective cloud objects identified in Part I.

A tropical deep convective cloud object (hereafter referred to as cloud object) is defined as a contiguous patch of cloudy regions that is composed of individual CERES footprints which satisfy the following criteria. First, the footprints must have 100% cloud fraction, i.e. all pixels within each footprint must be overcast. Second, the cloud optical depth and cloud top height of these footprints must be greater than 10 and 10 km, respectively. Third, the CERES footprints must be located over the Tropical Pacific Ocean between 25^oS and 25^oN. These identified cloud objects are further categorized into small-size, medium-size, and large-size cloud objects according to their equivalent diameters with the specified ranges of diameters given in Section 1. A total of 68 large-, 136 medium-, and 126 small-size cloud objects for the March 1998 period (part of the strong 1997/1998 El Niño), and 54 large-size cloud objects for the March 2000 period (weak La Niña) were identified in Part I. For simplicity, we denote the three different size categories of cloud objects observed during the March 1998 period as "L98", "M98", and "S98", respectively, and the large-size category observed during the March 2000 period as "L00". The average sizes of

cloud objects are 11600, 33400, 161700, and 127200 km^2 for S98, M98, L98, and L00 categories, respectively.

The cloud object data used in the present paper include outgoing longwave radiation (OLR), broadband TOA albedo, cloud optical depth (τ), cloud effective height, and cloud effective temperature. Histograms or probability density functions (PDFs) are used, instead of the areal means and standard deviations, to represent the statistical distributions of finer-scale characteristics of a cloud object. Summary PDFs of these observed cloud physical parameters for the four categories of cloud objects are used to compare with those analyzed from the CRM simulations in the present study.

3. CRM simulation design and analysis procedure

3.1 Model description

The model used in this study is the University of California at Los Angeles/Langley Research Center (UCLA/LaRC) CRM. This CRM is based on an anelastic dynamic framework (Krueger 1988; Xu and Krueger 1991) in two dimensions (x and z). It includes a bulk microphysics parameterization (Lin et al. 1983; Lord et al. 1984; Krueger et al. 1995), a third-order turbulence closure (Krueger 1988), and an interactive radiative transfer scheme (Fu and Liou 1993; Fu 1996; and Fu et al. 1998). Earlier versions of this CRM were used extensively for simulations of cloud processes and comparison with field experiment observations (Fu et al. 1995; Krueger et al. 1995 a, b; Xu and Randall 1996, 2000; Lin 1999 a, b).

The CRM's radiative transfer (RT) scheme has six and twelve spectral bands for solar and thermal IR regions, respectively. A generalized effective diameter (D_{ge}; see Fu 1996) is used as an input to the RT scheme and is related to the size distribution of the ice crystals. Both cloud ice and snow are treated together as ice crystals with respect to radiation calculation. The D_{ge} of the small ice crystals (cloud ice) depends on ice water content (IWC) (Q. Fu, pers. comm.):

$$D_{ge} = 192(IWC)^{0.331}, \quad (1)$$

where D_{ge} is in unit of μm, and IWC is in g m^{-3}. A constant D_{ge} of 120 μm was assumed for the large-size ice crystals (snow). When both cloud ice and snow exist in a grid box, a mass weighted D_{ge} is used. This formulation was also used in Xu (2005). The ocean surface spectral albedo is determined by solar zenith angle and surface wind speed using the parameterization of Jin et al. (2004). The mixing ratio of O_3 at each model level was interpolated from the standard tropical atmospheric profile (McClatchey et al. 1972). The concentration of CO_2 was assumed to be 330 ppmv.

3.2 Design of CRM simulation

In the present study, the simulations are designed to evaluate the CRM's ability to reproduce the observed properties for the three size categories of cloud objects in the Pacific that occurred in March 1998 and for the large-size cloud objects occurred in March 2000. Four ensembles of simulations are performed (Table 1) using a horizontal grid spacing of 2 km and a periodic horizontal domain. The width of the horizontal domain is 256 km for the S98 category, 512 km for the M98 and L00 categories, and 1024 km for the L98 category. These different domain sizes reflect the differences in the averaged sizes of observed cloud objects mentioned in Section 2. The vertical grid spacing is stretched below 5 km from 100 m near the surface to a constant 500 m above 5 km level in all simulations. The model vertical domain is 20 km with 46 layers. The model time step is 10 seconds.

The CRM was run for 24 h of physical time for each cloud object driven by large-scale tendencies of potential temperature and water vapor mixing ratio derived from European Center for Medium-range Weather Forecasts (ECMWF) analyses. These analyses were available every 6 hours on a 0.5625^o x 0.5625^o grid over the tropics, but they were spatially averaged over a rectangular area (up to 13x13 cells) that covers the observed cloud systems to be used for CRM input. The size of the rectangular area varies from one cloud object to another, depending upon its size

and shape. Each simulation is initialized from a horizontally homogeneous sounding that is obtained by averaging many ECMWF soundings over the rectangular area at a time (t_1) approximately 6 h before the cloud system was observed. The advective tendencies are averaged over the same area at two different times (t_1 and t_2) which are 6 h apart from each other. The later time (t_2) is closest to the satellite observation time of the cloud system. Tendencies at t_1 are used for the first 6 h and those at t_2 are used from 12 h to 24 h of the simulation. A linear interpolation of the tendencies at t_1 and t_2 is used to drive the model between 6 h and 12 h of the simulation. This setup is the same as that described in EX05. However, the domain-averaged horizontal wind at each model level is nudged toward the ECMWF sounding in the current study with the nudging time scale of 1 h. This was not done in EX05.

The advective forcings used to drive the CRM vary from one cloud object to another within a cloud object category. The variabilities as measured by standard deviations are comparable in magnitude to the means. The profiles of the advective tendencies averaged over all cloud objects within each category are shown in Fig. 1. The mean profiles show some similarities in their shapes among the four cloud object categories, particularly among the L98, M98, and S98 categories. All four profiles exhibit cooling in the entire troposphere and moistening except just above the surface. The magnitude of moistening and cooling generally increases with the size of the cloud objects during the March 1998 period, which is related to the different strengths of convective systems of different cloud object categories (Part II). In addition, the strength of the averaged cooling and moistening tendencies for the L00 category is located between those for the M98 and S98 categories in the upper troposphere, while it is about the same as that of S98 in the lower troposphere.

3.3 Sampling and analysis technique

A unified sampling and analysis method is used to examine each CRM simulation. Results from the last 12 h of the CRM simulations are sampled every 5 minutes, i.e. each simulation is sampled 145 times. The samples are then analyzed as described here. For each CRM grid column (2-km wide), we calculate the vertically integrated τ for the first visible band (wavelength of 0.2 to 0.7 μm). Integration starts from the model top and stops either where the integrated τ reaches 128 or at the 0^{o}C temperature level. A maximum τ of 128 is used because the CERES algorithm retrieves τ from observed solar reflectance which becomes saturated when τ is greater than 128. The 0^{o}C level is chosen because the satellite retrieval algorithm only considered ice clouds for this cloud type. Since the satellite saw reflected radiance which was an integrated effect by the atmospheric column, we include contributions from cloud ice, snow, and supercooled droplets in the integration of τ. We define a grid cell of the CRM as clear if its extinction ($\tau/\Delta z$) is less than 0.2×10^{-3} m^{-1} to remove partially cloudy cells produced by numerical noises, where Δz is the thickness of the grid cell, and cloudy otherwise. This means that a cloudy grid cell, with Δz of 500 m, must have $\tau > 0.1$. Only the cloudy cells are included in the integration of τ. Cloud top height (H_{ct}) for each CRM grid column is determined as the level where τ reaches one when integrated from the model top. This H_{ct} should be comparable to the "cloud effective height" derived by CERES based on a recent study of Holz et al. (2006). Temperature at the height of H_{ct} is determined as the cloud top temperature (T_{ct}) and should be compared with the CERES "cloud effective temperature".

As described in Section 2, the CERES SSF data have an average footprint size of about 10x10 km^2. In order to better match the CRM results based on 2 km grid to the actual CERES cloud object footprint data, a 12 km running average (i.e. six grid columns) is applied to the simulated cloud physical properties. Only those 6-grid areas that (1) are overcast, (2) have a mean H_{ct} greater than 10 km, and (3) have a mean τ greater than 10 are identified as candidate deep convective cloudy areas. These candidate areas include a few columns with lower cloud tops near the

edges of a deep convective cloud. Since the observed cloud top heights within each CERES footprint have a standard deviation generally less than 10% of the mean H_{ct} averaged over the footprint, we further exclude any candidate area if the cloud top heights within each of the 6-grid area satisfy both of the following conditions: a) the standard deviation of H_{ct} is greater than 10% of the mean H_{ct}; b) the minimum H_{ct} is less than 10 km and less than 80% of the mean H_{ct}. The means of cloud properties at these selected deep convective areas are then used to construct the PDFs for each simulation. The summary PDF of a certain cloud physical parameter is obtained from the PDFs of individual simulations within each ensemble.

The differences between two summary histograms are quantitatively represented by the Euclidean distance (also called L2 distance). A bootstrap procedure is then applied to determine whether the difference between two summary histograms is statistically significant, as proposed by Xu (2006). The null hypothesis for the test is that all cloud objects came from the same population for a certain parameter. This procedure consists of four steps. First, the L2 distance between the two summary histograms of a particular parameter is calculated, which is called the measured L2 distance; Second, all individual histograms contained in the two summary histograms under test are combined to form one group. Third, two sets of histograms are formed through random selection of the individual histograms in this group, each with the same number of histograms as the two original summary histograms. A randomized L2 distance is calculated from the two sets of the randomly generated summary histograms. This distance is then compared to the measured L2 distance. This step is repeated 10,000 times. Lastly, the frequency that a randomized L2 distance is as great as or greater than the measured L2 distance is calculated, which is denoted as the p value. The p-statistic provides a measure of the probability that the two PDFs are from the same statistical distribution. Therefore, (1-p) is the confidence with which we can claim that the two PDFs are from different statistical distributions. For p=0.01, we have 99% confidence that the two PDFs are significantly different. The threshold p value is customarily chosen to be 0.05.

4. Comparison of large-size cloud objects between March 1998 and March 2000

4.1 Vertical profiles of cloud fraction and hydrometeor mixing ratio

The model-simulated vertical profiles of cloud fraction and hydrometeor mixing ratio contain essential information for understanding the behavior of simulated PDFs of cloud parameters. Therefore, these results are presented first. The vertical profile of the temporally averaged cloud fraction of the large-size category generally has smaller values during March 2000 than that during March 1998 (Fig. 2a), due to the weaker large-scale forcings in the March 2000 period (i.e. the L00 category in Fig. 1). Both categories have two vertical peaks located at 12.5 km and 2 km, corresponding to upper troposphere anvil and shallow cumulus, respectively.

The vertical profiles of the temporally- and horizontally-averaged hydrometeor mixing ratios for the L00 simulations are generally smaller than those for the L98 simulations (Fig. 3). However, at heights above ~16 km, the L00 category has a greater mixing ratio of ice-phase hydrometeors than the L98 category (Fig. 3f), consistent with its greater cloud fractions at the same height range (Fig. 2a). The larger mixing ratios of the L00 category at heights above 16 km are consistent with the large instabilities of the initial soundings as will be shown in Section 4.3. Cloud ice, snow, and graupel exist above the freezing level in the CRM. The peaks of their vertical profiles are located at 10 km, 8 km, and 5 km, respectively, stratified by their different fall speeds and the roles of different microphysical processes. Supercooled liquid water exists at heights up to 10 km. These characteristics are similar to those obtained by other CRMs for tropical convection (e.g., Tao et al. 2003; Johnson et al. 2004; EX05).

4.2 Comparison of PDFs between the CRM results and CERES observations

In this section, the ability of the CRM to produce realistic distributions of cloud physical properties is examined. To accomplish this, the statistical distributions of selected cloud physical parameters are compared between the CRM simulations and the CERES observations for the large-size cloud objects that observed during two climatologically distinct periods.

Three cloud macrophysical parameters, cloud top height, cloud top temperature and OLR, are examined as a group because they are closely related to each other for the type of cloud systems examined in this study, i.e., optically thick clouds with tops above 10 km. Any significant difference or similarity in one parameter from the observed distribution also appears in the distribution of another parameter. First, it is easily seen that the simulated probability density of H_{ct} with values between 10 and 11.75 km agrees well with that of the observed for the L98 category (Fig. 4a), so do T_{ct} with values between 230 and 250 K (Fig. 4c) and, to less extent, OLR with values between 140 and 170 W m^{-2} (Fig. 4e). These relatively lower-top clouds have moderate to large optical depths, due to contributions from supercooled liquid water. Second, the differences from observations associated with higher-top clouds are pronounced in all three parameters for the L98 category, i.e., the overestimate of probability density in the middle range of the distributions (11.75 - 13.25 km for H_{ct}, 118 - 140 W m^{-2} for OLR, and 215 - 230 K for T_{ct}) and underestimate of probability density in the upper range of H_{ct} (> 13.25 km) and the lower ranges of OLR (90-118 W m^{-2}) and T_{ct} (200-215 K). This result means that the simulated high clouds are too low, compared to the observed. A detailed explanation for this result is given below.

EX05 used a different CRM (2-D version) to simulate the same L98 category of cloud objects using identical advective forcing and initial sounding data as in this study. They also underestimated the cloud top heights, i.e., there were very few occurrences of clouds with tops over 14.25 km. This may suggest that the imposed large-scale forcings may contribute to the underestimate of cloud top height. The imposed large-scale forcings are generated from the ECMWF analysis and may have some uncertainties (Xie et al. 2003). During the March 1998 period, a majority of cloud objects occurred in the data-sparse central and eastern Pacific regions as discussed in Part I; that is, there are few radiosonde measurements for input to ECMWF data assimilation. The exact extent of the uncertainties cannot be quantified, however. On the other hand, it is well-known that cloud-scale dynamics impacts the organization of mesoscale cloud systems and well-organized convection has well protected convective cores which penetrate

higher. The two dimensionality of the CRM may also contribute to deficiencies in its simulated mesoscale structures and hence cloud top heights.

In contrast to those of the L98 category, the three cloud macrophysical properties of the L00 category are reasonably reproduced in the middle ranges of the distributions (12.5-14.5 km in H_{ct}, 205-220 K in T_{ct}, and 95-120 W m^{-2} in OLR), but the probability densities for the lower-top clouds are underestimated and those for the very high clouds are overestimated (Figs 4b, 4d and 4f). Why does the CRM produce such different results for a different period? One possible reason, as will be shown in Section 4.3, is the increases of convective instability in the initial soundings of L00, which favors the initiation of deeper convective clouds if the advective forcings are identical. A precursor of this result is the slightly larger cloud ice mixing ratio above 15 km in L00 than in L98 (Fig. 3a).

The differences in the cloud macrophysical properties from the observations obviously impact the cloud optical depth and TOA albedo. There is, however, no one-to-one relationship between cloud macrophysical properties and cloud optical depth because clouds with the same top heights may have different optical depths due to different cloud base heights and amounts of super-cooled liquid water and ice crystals. Figures 5a and 5b show the observed and model-simulated τ distributions for L98 and L00, respectively. While both the observed and simulated τ have exponential distributions, the simulated distributions have higher probability density (~0.05) at the smallest τ than the observed distributions (~0.03). Furthermore, the simulated cloud objects have fewer occurrences of large cloud optical depths ($\tau > 80$ in L98 and $\tau > 60$ in L00), partially related to the underestimated high-top clouds ($H_{ct} > 13.5$ km) in L98 and low-top clouds ($H_{ct} < 12.5$ km) in L00. These disagreements between the simulated and observed τ may also suggest that the effective sizes of ice crystals used for the radiative transfer (RT) calculation in the simulations are too large. The larger effective size of ice crystals may also affect the simulated distribution of TOA albedo as discussed below.

Figures 5c and 5d show the observed and model-simulated distributions of TOA albedo for L98 and L00, respectively. While the distributions of the observed TOA albedo have a shape that is nearly Gaussian with a mode at 0.625 and 0.675 for the L98 and L00 categories, respectively, the simulated albedo distributions are significantly different from those observed. A striking feature is that the simulated albedo distributions lack values greater than ~0.7. This is consistent with the underestimate of large τ values in the simulations as discussed earlier. The differences between the simulated and observed distributions of albedo are probably related to uncertainties in the ice-phase cloud microphysics and RT calculation in the CRM. Further discussion of this issue will be given in Section 8.

4.3 Comparison of observed and simulated differences between March 1998 and March 2000

In this section, the ability of the CRM to simulate the observed differences/similarities between the large cloud objects of March 1998 and March 2000 is examined. To do this, the simulated differences between the cloud property distributions of L98 and L00 are compared to the observed differences between the two periods.

The observed cloud top heights differ most significantly among the selected parameters between the two periods, as indicated by the smallest p value of 0.1% (Table 2). The observed cloud tops during March 1998 (the 1997/98 El Niño) were higher than those during March 2000 (weak La Niña) (Fig. 6a). The modes of the distributions differ by 0.5 km between these two periods with the higher mode (12.75 km) occurring in March 1998. These differences are associated with the significant changes in the stratification of the troposphere as well as changes in the SST distribution that occurred during the El Niño event (Part I). Figure 6b shows that the probability densities of the simulated cloud tops below 11.5 km for the L00 category are higher than those for the L98 category, consistent with the CERES SSF data. However, for cloud top heights above 13 km, the simulations did not reproduce the significant differences in the occurrences of cloud tops between the two periods seen in the observations. In contrast to the observations, the simulated distributions of H_{ct} have the same mode of 12.75 km for both periods. This lack of difference in

the simulated cloud top height may due partly to the lower/higher CAPE values for the L98/L00 cloud objects. Since the ascending ability of the near-surface air parcels would directly affect H_{ct} as suggested by the parcel theory, one may expect a direct link between the initial soundings used in the simulations and the simulated cloud top heights. Therefore, we computed the pseudoadiabatic convective available potential energy (CAPE) using the initial soundings and determined the cumulative probability of the CAPE for each ensemble of the simulations (Fig. 7). The initial soundings for the L00 category have larger CAPEs than any size category in the March 1998 period. Nineteen out of 54 cloud objects of the L00 category have CAPEs greater than 1500 J kg^{-1} while almost none of the soundings during the March 1998 period has such a large value of CAPE. The small/large initial CAPEs for the L98/L00 category may thus contribute to its lower/higher simulated cloud tops than the observations.

Despite the significant differences in H_{ct}, the observed T_{ct} (Fig. 6c) and OLR (Fig. 6e) distributions only differ moderately between the March 1998 and March 2000 periods, due to changes that occurred in the stratification of the troposphere. The observed distributions between the two periods are essentially the same for low T_{ct} (< 210 K) and OLRs (< 100 W m^{-2}). However, the simulated T_{ct}s (Fig. 6d) and OLRs (Fig. 6f) differ significantly between the two periods with more low OLRs and T_{ct}s simulated for L00 than for L98. This may appear to be inconsistent with the simulated cloud top heights, which show essentially identical distributions for H_{ct} greater than 13.5 km. A closer examination indicates that the stratifications of the model atmosphere associated with the two periods are quite different. The lapse rates associated with the L00 category are greater than those of the L98 category. This fact leads to lower T_{ct} and OLR even though the distribution of H_{ct} remains relatively unchanged. The different atmospheric stratifications between the simulations for L98 and L00, determined by the ECMWF analyses, reflects the greater amount of convective activity during the 1997/98 El Niño event, which acted to stabilize the atmosphere more efficiently than during the weak La Niña period. In addition, the modifications made to the physical parameterizations and the vertical resolution of the ECMWF model in 1999

(http://www.ecmwf.int/products/data/technical/model_id/) could also contribute to the differences in the ECMWF analyses between the two periods.

The observational and the model simulated differences in τ and albedo between these two periods are very consistent with each other. The observations show essentially no difference in τ (Fig. 8a) and albedo (Fig. 8c) between the two periods, as indicated by the p values of 74.2% and 95.9%, respectively (Table 2). This suggests that the distributions of τ and albedo of the identified cloud objects are not significantly influenced by changes in the large-scale circulations and SST distributions. The CRM simulated τ (Fig. 8b) and albedo (Fig. 8d) also do not differ significantly between the two categories of cloud objects. The p values are 52.2% and 19.4% for τ and albedo, respectively (Table 2).

5. Comparison among the three size categories during March 1998

5.1 Vertical profiles of cloud fraction and hydrometeor mixing ratio

Figure 2b shows the vertical profiles of cloud fraction from the simulations of the L98, M98, and S98 categories. The temporally and horizontally averaged cloud fractions generally increase with the size of cloud objects, due to the increasing strength of the forcings used to drive the CRM (Fig. 1). As mentioned in Section 4.1, the simulations of the L98 cloud objects produced two peaks in the average profile of cloud fraction: the peak for upper tropospheric anvils is located at 12.5 km and the other peak represents shallow cumulus at 2 km. A third peak, located at ~7 km, is more pronounced in the vertical profiles of the M98 and S98 categories of cloud objects and this peak represents congestus cumulus (Johnson et al. 1999). The forcings used to simulate the smaller-size cloud objects are weaker than those for the large-size cloud objects during the March 1998 period (Fig. 1). This may create an environment for the M98 and S98 simulations that is favorable for the production of congestus cumulus.

For the three size categories of cloud objects, the mean hydrometeor mixing ratios increase with the size of cloud objects (Fig. 9), consistent with the cloud fractions. The profiles for each type of hydrometeor, as well as for the sum of all hydrometeors, show generally similar

shapes among the three size categories. However, there are no observations available to verify these results.

5.2 Comparison of PDFs between the CRM results and CERES observations

For each of the three size categories of cloud objects, the L2 distances and p values are computed for the selected parameters using their PDFs from the observations and simulations to facilitate direct comparison between them (Table 3). We also compare the distributions among the three size categories for both the observations (Table 4) and the simulations (Table 5) to examine the CRM's ability to simulate the observed differences among the three size categories. The simulated and observed PDFs of H_{ct}, OLR, TOA albedo, and τ are illustrated in Fig. 10.

5.2.1 Cloud top height, OLR, cloud top temperature

It is found that the observed cloud top heights differ significantly between any pairs of two different size categories (Fig. 10b). The differences are more significant between the large- and small-size categories than those between the small- and medium-size categories or between the large- and medium-size categories. The H_{ct} distributions also shifted toward greater values with increasing size of cloud objects. As a result, the modes of the distributions differ by 1.5 km between the large- and small-size categories. The higher cloud tops for larger-size cloud objects are indicative of the stronger convection associated with the large-size cloud objects. The simulations reproduced the greater differences between the L98 and S98 categories than those between the L98 and M98 or between the M98 and S98 categories, as seen in the observations. The tendency for more occurrences of lower cloud tops (for example, below 11.5 km) in the simulated S98 distribution (Fig. 10a) is also consistent with the observations. However, a shortcoming of the simulations is their inability to produce the significant differences in H_{ct} among the size categories as shown in the observations. This results from an underestimate of higher clouds for the large-size category and an overestimate of higher clouds for the smaller-size categories by the CRM simulations.

The model's inability to capture the increase in H_{ct} with cloud object size is probably related to the way in which the forcing data were averaged. For the larger cloud objects, there tends to be a larger amount of variation in the strength of forcing within the rectangular area over which the average forcing is calculated than for the smaller cloud objects. In the real atmosphere, the highest cloud tops within a cloud system are presumably associated with the strongest advective forcings, which are smoothed out by the spatial averaging. On the other hand, there are considerable numbers of cloud objects in the M98 (25) and S98 (37) categories that produce small deep convective areas (~1%). This means that these cloud objects do not contribute much to the simulated summary histograms, but do contribute to the observed summary histograms. The forcings for these cloud objects are generally weaker than those for other cloud objects within the same category, resulting from mismatch in time and spatial location of cloud objects between the ECMWF model and the CERES observation. If we exclude the simulations that produced small deep convective areas, the forcings averaged over the remaining simulations are stronger than those averaged over the entire M98/S98 ensemble while remain almost the same for L98. Therefore, the simulated summary histograms of M98 and S98 are heavily skewed by those cloud objects with strong advective forcings which produce high cloud tops, contributing to the lack of difference among the three size categories.

It is obvious that the observed OLRs between the L98 and S98 categories differ more significantly than those between the L98 and M98 or between the M98 and S98 categories (Fig. 10d). Although the observed OLRs exhibit two modes for all three size categories, the mode with the value of ~124 W m^{-2} is less pronounced for the small-size category than for the large- and medium-size categories. In addition, the other mode with the value of 140 W m^{-2} is the most pronounced for the S98 category and the least pronounced for the L98 category. This suggests that a larger fraction of clouds with relatively lower tops (and warmer temperatures) were observed for the small-size cloud objects than for the larger-size cloud objects, consistent with the differences among the three size categories found in the observed H_{ct} (and T_{ct}).

Figure 10c shows that the simulated OLRs have approximately Gaussian distributions. The differences in the simulated OLRs between the L98 and S98 categories are more significant than the difference between the L98 and M98 or between the M98 and S98 categories. Higher probability densities of large OLRs (greater than 150 W m^{-2}) can be seen in the S98 category than the larger-size categories. All of these features are consistent with the observed PDFs. However, the simulated OLRs do not differ among the three size categories as significantly as those observed. In particular, the left halves of the OLR distributions show nearly identical probability densities among the three size categories. This is consistent with that shown in H_{ct} in the higher cloud-top range. The same physical interpretation given earlier for the deficiencies in the simulated distributions of H_{ct} also applies for OLR.

The observations suggest that distributions of T_{ct} (not shown) differ significantly among the size categories. The single mode of the nearly Gaussian distributions shifts toward larger T_{ct} with decreasing cloud object size. As a result, the mode of S98 (230 K) is greater than that of L98 by 10 K. The p values (Table 5) suggest that the simulations produced more significant differences between L98 and S98 than those between M98 and S98 or between L98 and M98, consistent with the observations, as in OLR (Figs. 10c, d).

5.2.2 TOA albedo and cloud optical depth

The observed TOA albedos have nearly Gaussian distributions (Fig. 10f), which differ significantly between the large- and small-size, moderately between the medium- and small-size, and insignificantly between the large- and medium-size categories. The distributions of the simulated TOA albedo appear to be similar among the three size categories (Fig. 10e). They all have the shape of a triangle that is tilted towards the right side (larger values). Compared to the observations, too few large albedos (greater than 0.7) were simulated for the three size categories resulting in more narrow ranges of the simulated distributions. Too few small albedos (less than 0.55) were generated by the simulations for the medium- and small-size categories, although the lower limit of the simulated TOA albedo is the same as that of the observations (~0.4). As previously mentioned in Section 4.2, uncertainties in the ice-phase cloud microphysics and RT calculation in

the CRM are a possible cause for these differences between the simulated and observed TOA albedos. A detailed discussion will be given in Section 8. In spite of the significant differences between the observations and simulations, a tendency that the simulated albedos decrease with decreasing size of the cloud objects can be seen in Fig. 10e, although it is much less obvious than that in the observations (Fig. 10f).

The cloud optical depths exhibit exponential distributions, an observed characteristic reproduced well by the simulations (Figs. 10g, h). However, the simulations overestimate the probability density at the smallest values of τ versus the observations, particularly for the large-size cloud objects. The observed probabilities increase slightly near the end of the right tail because the retrieved τ was assumed to be less than 128 when the retrieval algorithm could not confidently determine the large τ values (see Section 8). This feature is not seen in the simulated distributions although we limited the τ to be less than 128 for each of the CRM grid column (Section 3.3). The histograms of τ for the M98 and S98 categories do not differ significantly from the observations as suggested by the p values of ~12% (Table 3). However, this agreement between the simulated and observed τ distributions for M98 and S98 may result from a cancellation between the excessively large cloud top heights (leading to a large τ) and effective sizes of ice crystals that are too large (leading to a small τ) in the simulations.

6. Sensitivity analysis

6.1 Effects of analysis methods

So far, we have shown simulated PDFs of cloud properties that were averaged over six grid columns in order to match with the average size of the CERES footprints on board the TRMM satellite. To test the effects of using a running mean average (RMA) on the simulated PDFs, we conducted an analysis (denoted by COL) that did not use any averaging for the four categories of cloud object. The COL analysis calculates all fields at each column in the same manner

as in Section 3.3, but constructs histograms of the fields based on the individual columns rather than the averaged columns. The latter is referred to as the RMA analysis.

The resulting distributions of H_{ct} (Fig. 11a), OLR (Fig. 11b), and T_{ct} from COL for L98 were quite similar to those from RMA, probably because the horizontal scale of the simulated anvils is larger than 12 km. As expected, τ from COL has larger probability densities at the smallest and greatest values of bin and smaller probability densities in the range between 30 to 100 (Fig. 11c). Albedos from COL have smaller probability densities in the range between 0.55 to 0.65 but larger probability densities at values greater than 0.70 (Fig. 11d). The larger probability densities of the COL albedo at large values (> 0.7) tend to agree better with the observations, resulting in a smaller L2 distance (Table 6). Similar results of these parameters are also found for the M98, S98, and L00 categories (not shown), respectively.

Another analysis method to be compared with was proposed by Eitzen and Xu (2005; EX05). Their method to analyze the simulations is similar to COL. However, they integrated down to the surface to determine τ and excluded the columns that have an optically-thin (τ < 10) top cloud layer overlying lower clouds even if the total column τ is greater than 10. To compare our results with those of EX05, we conducted another analysis (denoted by EX) for the L98 category using the same method as described in EX05. The L2 distances between the summary PDFs from the observations and CRM results (COL and EX, respectively) and the corresponding p values, as well as those from EX05, are provided in Table 6.

The histograms from COL and EX are generally similar for most parameters except for τ. Figure 11c shows that the τ histogram from EX has smaller probability densities at the small values (< 20) and higher probability densities at the high values (> 60) than COL, probably because EX included contributions of cloud droplets below the freezing level while COL did not. The L2 distances between simulated and observed PDFs presented in this study are smaller than those from EX05. In particular, the L2 values for OLR, H_{ct}, and T_{ct} from RMA, COL and EX are less than half of their counterparts from EX05. Therefore, we conclude that our CRM results for the

large-size category of March 1998 generally agree more closely with the observations than EX05, whether we use the same or different methods to analyze the CRM fields. The closer agreement is due to the anelastic dynamic framework and third-order turbulence closure used in the UCLA/ LaRC CRM. This is because both sets of simulations were initialized from the same soundings and driven by the same advective forcings. Both CRMs employed the identical ice-phase microphysical and radiative transfer schemes but different dynamic frameworks and turbulence closure schemes.

6.2 Effects of ice effective size formulations

As discussed in Sections 4 and 5, uncertainties associated with some simulated cloud properties are probably related to the effective size of ice crystals (D_{ge}) as input to radiation calculation. The CRM simulations used a D_{ge} formulation that is a function of IWC only, $D_{ge}(IWC)$ (Eq. 1), based on limited in situ aircraft observations of small ice crystals inside cirrus clouds (Fu 1996). Two new formulations of D_{ge} are constructed and used to simulate the L98 category to explore the effects of D_{ge} formulation on simulated cloud properties. One is a function of temperature, $D_{ge}(T)$, and the other is a function of both IWC and temperature, $D_{ge}(IWC, T)$. The former is based on the data from Boudala et al. (2002) and Garrett et al. (2003) (Fu, pers. comm., 2006):

$$D_{ge}(T) = 47.05 + 0.6624T + 0.001741T^2, \quad (2)$$

where T is temperature in centigrade. The latter is based on observations acquired from several field programs (Heymsfield et al. 2005):

$$D_{ge}(IWC, T) = 192(IWC)^{0.331}\left(0.5 + \frac{T - T_1}{T_2 - T_1}\right), \quad (3)$$

where T_1 and T_2 equal -80^{o}C and 0^{o}C, respectively. Figure 12 shows the dependence of D_{ge} on IWC and T from (1), (2) and (3). $D_{ge}(IWC, T)$ increases by a factor of 3 with increasing temperature from T_1 to T_2 (Fig. 12b). $D_{ge}(IWC, T)$ equals $D_{ge}(IWC)$ at a temperature of -40^{o}C. For any temperature between -70^{o}C and -10^{o}C, the dependence of D_{ge} on IWC from $D_{ge}(IWC, T)$ is consistent with Fig. 2 of Heymsfield et al. (2005).

The resulting summary histograms of four cloud properties are compared among the three sets of simulations with $D_{ge}(IWC)$, $D_{ge}(T)$, and $D_{ge}(IWC, T)$, and with the CERES observations (Fig. 13). With the $D_{ge}(IWC, T)$ formula, the simulated PDFs of H_{ct}, T_{ct}, and OLR lie between those obtained with $D_{ge}(IWC)$ and $D_{ge}(T)$ formulae, and they agree with the CERES observations better. This is due to smaller $D_{ge}(IWC, T)$ than $D_{ge}(IWC)$ near the cloud tops where the temperatures are mostly colder than -40^{o}C (Fig. 4c), which increases τ and the estimated cloud top height based on τ and cloud emissivity (thus smaller OLR). It is also noted that the PDFs of τ and TOA albedo do not differ significantly between the $D_{ge}(IWC)$ and $D_{ge}(IWC, T)$ simulations because $D_{ge}(IWC, T)$ is greater than $D_{ge}(IWC)$ for temperature between 0^{o}C and -40^{o}C.

With the $D_{ge}(T)$ formulation, the CRM generated larger probability densities for large τ, high TOA albedo, small OLR, and high cloud tops (Fig. 13). This is expected since $D_{ge}(T)$ is generally smaller than either $D_{ge}(IWC)$ or $D_{ge}(IWC, T)$ (Fig. 12). The unrealistically high densities at high albedo from the $D_{ge}(T)$ simulation suggest that the $D_{ge}(T)$ formula may produce ice crystal diameters that are too small for the deep convective clouds. The higher cloud tops from this simulation are simply because we define the cloud top as the level where τ, when integrated from the top of the atmosphere, reaches one to be consistent with the CERES retrieved cloud-top height. With smaller values of D_{ge} and hence larger τ, the cloud tops are higher even with similar

profiles of cloud ice mixing ratios. It is indeed found that the horizontally- and temporally-averaged hydrometeor mixing ratios change very little (not shown). This result suggests that the different D_{ge} formulae have little effect on the simulated cloud microphysical properties.

7. Summary

The MMF approach for climate modeling uses a CRM embedded within each grid cell of a GCM to replace most conventional parameterizations used in traditional GCMs. Climate simulations conducted using this approach are therefore significantly influenced by the embedded CRM. The present study has attempted to evaluate the ability of the UCLA/LaRC CRM, which is currently being implemented into a GCM for climate study, in simulating tropical deep convective cloud systems. Our strategy is similar to that outlined in EX05: to drive the CRM using the ECMWF forcing data, which are matched with the large ensembles of tropical deep convective cloud objects observed by the TRMM satellite; to analyze the statistical properties of the CRM-simulated deep convective clouds in terms of summary histograms, which provide fine-scale information of cloud properties for each category of cloud objects classified by their equivalent diameters and/or climate regimes; and to compare these histograms with those of observed cloud objects from the CERES SSF data to identify possible causes for the disagreements and to suggest future improvement to the CRM. This strategy will lead to an improved MMF, as detailed in Part I.

The CRM is used to simulate the three size categories of tropical deep convective cloud objects observed during March 1998 (strong El Niño) and the large-size category observed during March 2000 (weak La Niña). These observed cloud objects were identified from the TRMM CERES SSF data in Part I of this series of study using an objective classification technique. In order to compare with the observed cloud object data, cloud properties from the CRM simulations are sampled and diagnosed in a way that is consistent with the CERES retrieval algorithms and matches with the average scale of the CERES satellite footprints (10 x 10 km^2). Histograms of cloud physical parameters including cloud top height, cloud top temperature, OLR, TOA albedo,

and cloud optical depth are then computed for the four ensembles of simulations and have been compared to those of satellite cloud object data. The differences between each pair of summary histograms are measured by the Euclidean distance and their statistical significance is determined by a bootstrap procedure (Xu 2006).

There is a general agreement in the overall shapes between the simulated and observed PDFs. Each cloud physical property produced by the CRM also exhibits different degrees of disagreement with the observations over different ranges of the property. The simulated cloud tops are generally too high and cloud top temperatures are too low except for the large-size category of March 1998. Probability densities of TOA albedos for all four categories are underestimated in the high range and those of τ are overestimated at its lowest bin. However, these disagreements are smaller than those found in a similar study by EX05 using a different CRM for the same large-size category of March 1998. Sensitivity analyses suggest that the major conclusions are basically not changed whether or not the running averaging is applied to the CRM fields.

It is found that the observational and the model-simulated differences in cloud optical depth and albedo between the two observational periods are very consistent with each other. They are not significantly influenced by changes in the large-scale circulations and SST distributions. However, the CRM underestimates the significant differences in the observed cloud top height while it overestimates the differences in the observed OLR and cloud top temperature between the two periods. In terms of the relationships among the three size categories of cloud objects observed during March 1998, the CRM simulations generated the same more significant differences for most parameters between the large- and small-size categories than between the large- and medium-size, or between the medium- and small-size categories as the observations. However, the simulated cloud properties do not change as much with cloud object sizes as observed. These results are related to both the dilution through spatial averaging of the advective forcings which disproportionally affects the large-size category and the mismatch between the observed cloud objects and the ECMWF analyses in time and in space for the small- and medium-size categories.

It should be noticed that the domain size and horizontal and vertical grid spacings of CRMs used in MMFs are different from those used in this study. Some of the cloud properties examined in this study are likely impacted by different selections of these specifications in an MMF. We plan to examine these issues in a separate study.

8. Discussion

The major causes for the disagreements of the simulated cloud properties with observations are uncertainties associated with the CRM simulations, as mentioned in previous sections and further summarized here. The PDFs of TOA albedo differ more significantly than other parameters between the CRM simulations and CERES SSF data, regardless of the size categories of cloud objects and the climate regimes in which the cloud objects occurred. The CRM underestimated the occurrences of high albedos (greater than 0.7) for all categories of cloud objects, as well as the occurrences of low albedos (less than 0.55) for the L00, M98, and S98 categories of cloud objects. There are a few possible causes for the significant differences seen between the simulated and observed PDFs. The first cause could be the excessively large effective sizes of ice crystals (cloud ice and snow). They can result from too little simulated cloud ice instead of simulated snow and/or graupel due to deficiencies in the CRM's one-moment bulk microphysical parameterization or from the empirical formula of D_{ge} that was based on limited in situ aircraft observations of small ice crystals inside cirrus clouds (Fu 1996). The D_{ge} formula may not be representive of the actual size distribution of ice crystals in the tropical deep convective clouds. This aspect has been extensively discussed in Section 6.2. A possible remedy is to implement a two-moment bulk cloud microphysics scheme in the CRM, which can more physically determine the effective size of hydrometeors. Such work is being carried out. The second cause for albedo differences between the simulations and observations can be related to the application of independent column approximation (ICA) to the CRM simulations. ICA uses a plane-parallel radiation model to calculate radiative flux for each column so that the 3-D geometry impacts of clouds on radiative transfer are neglected. Ignoring 3-D geometry impacts of clouds on solar radiative trans-

fer is probably inappropriate for tropical deep convective clouds (e.g., Fu et al. 2000). The third cause for albedo differences is that the observed albedo increases with increasing solar zenith angle (SZA) given the same cloud microphysical and macrophysical properties. However, at each time step of a simulation, a single SZA at the center of the observed cloud object was used for radiation calculation at all grid points in the CRM domain. That is, SZA varies within an observed cloud object but it is held constant within the CRM domain for each simulation. This can cause relatively minor differences between the simulated and observed albedo, but it affects the larger cloud objects more than the smaller ones.

While the differences between the simulated and observed distributions of albedo are mainly related to uncertainties associated with the ice-phase cloud microphysics and RT calculation in the CRM, the difference between the observed and simulated H_{ct}, T_{ct}, and OLR are tightly related to uncertainties in the forcing and initial sounding data for the CRM simulations, as discussed in Section 5. For example, the horizontal variabilities of these data were averaged out, especially the extreme values of forcing inside the rectangular area that covers a cloud object and its surrounding environment. This probably contributed to the lack of difference in most parameters among the three size categories. There is mismatch in time between the forcing data and the observations because the ECMWF analyses were available every 6 h. This time-mismatch could contribute to the disagreements seen between the observed and simulated histograms. Also, the observed cloud objects were located in data sparse oceanic regions. This could impact the quality of the ECMWF analyses.

The disagreements of all simulated cloud properties with observations could be related to the fact that the CRM simulates the physical processes in 2-dimension (x-z) and therefore may not be able to capture the complete characteristics of the observed tropical deep convective cloud systems. The closer agreement of the present study with the observations than EX05 also suggests that dynamic framework and turbulence closure scheme could impact all simulated cloud properties.

The disagreements seen in the observed and simulated PDFs can also be caused by various degrees of uncertainties associated with the parameters included in the CERES SSF data, particularly the systematic errors (Xu et al. 2006). The observed OLR and SW fluxes were converted from broadband radiance measurements using the CERES Angular Distribution Models (Loeb et al. 2003). The albedo was calculated by taking SW flux divided by theoretical solar insolation at the footprint location and time. Wielicki et al. (1996) gave an estimate of the CERES instantaneous flux error which is 12.9 and 4.3 W m^{-2} for the SW and LW, respectively.

The CERES cloud effective temperature was derived from imager radiances at the IR channels. The retrieval of cloud effective temperatures is relatively more accurate for the optically thick high-top clouds examined in this study than for thinner clouds. Since the cloud effective height was determined as the height of the level at which the ECMWF analyses had the same temperature as the cloud effective temperature, the uncertainties in the retrieved cloud effective heights could be caused by possible errors in the ECMWF analyses.

The CERES cloud optical depth was retrieved from solar reflectance in the visible channel (0.65 μm) of cloud imager. Ice crystals are nonabsorbing at the visible channel. Photons transported within a cloud can undergo numerous scattering events deep into the cloud and still emerge from cloud top. The visible reflectance is thus enhanced as τ increases. The retrieval of τ is fairly reliable even without accurate information on effective size of ice crystals (e.g. Rossow et al. 1989). However, the rate of change in reflectance due to the increase of τ becomes slower as τ increases. Therefore, τ greater than a certain value could not be physically retrieved. The maximum reliable value of τ for each imager pixel in the CERES footprint was assumed to be 128. This limitation is a source of uncertainties in the upper range of τ PDFs.

The results from this study indicate that additional information is needed to further constrain model simulations, in particular, the vertical distributions of ice crystal mass and the ice size distributions in convective clouds. Such observational data are becoming available through the Cirrus Regional Study of Tropical Anvils and Cirrus Layers - Florida Area Cirrus Experiment

(e.g. Wang et al. 2005) and will also be provided by CloudSat (Stephens et al. 2002) and CALIPSO (Winker et al. 2003).

Acknowledgments. This research was supported by the NASA EOS interdisciplinary study program (Dr. Donald Anderson, Program Manager). The CERES data were obtained from the Atmospheric Sciences Data Center at the NASA Langley Research Center. Many thanks to Mark Branson at Colorado State University for providing the advective cooling and moistening tendency data and Lindsay Parker of SAIC for deducing the cloud object data from the CERES SSF data. We appreciate Dr. Andrew J. Heymsfield of National Center for Atmospheric Research and two anonymous reviewers for their valuable comments that helped to clarify and improve this paper. Discussion with Drs. Yongxiang Hu and Wenbo Sun of NASA Langley Research Center and Dr. Shaocheng Xie of Lawrence Livermore National Laboratory is also appreciated.

References

Ackerman, T., and G. M. Stokes, 2003: The Atmospheric Radiation Measurement Program. *Physics Today*, **56**, 38-45.

Arakawa, A., 2004: The cumulus parameterization problem: Past, present, and future. *J. Climate*, **17**, 2493-2525.

Boudala, F. S., G. A. Isaac, Q. Fu, and S. G. Cober, 2002: Parameterization of effective ice particle size for high-latitude clouds. *Int. J. Climatol.*, **22**, 1267-1284.

Eitzen Z. A., and K.-M. Xu, 2005: A statistical comparison of deep convective cloud objects observed by an Earth Observing System satellite and simulated by a cloud-resolving model. *J. Geophys. Res.*, **110**, D15S14, doi:10.1029/2004JD005086.

Fu, Q., 1996: An accurate parameterization of the solar radiative properties of cirrus clouds for climate models. *J. Climate*, **9**, 2058-2082.

Fu, Q., and K. N. Liou, 1993: Parameterization of the radiative properties of clouds. *J. Atmos. Sci.*, **50**, 2008-2025.

Fu, Q., S. K. Krueger, and K. N. Liou, 1995: Interactions of radiation and convection in simulated tropical cloud clusters. *J. Atmos. Sci.*, **52**, 1310-1328.

Fu, Q., P. Yang, and W. B. Sun 1998: An accurate parameterization of the infrared radiative properties of cirrus clouds for climate models. *J. Climate*, **11**, 2223-2237.

Fu, Q., M. C. Cribb, H. W. Barker, S. K. Krueger, and A. Grossman, 2000: Cloud geometry effects on atmospheric solar radiation. *J. Atmos. Sci.*, **57**, 1156-1168.

Garrett, T. J., H. Gerber, D. G. Baumgardner, C. H. Twohy, and E. M. Weinstock, 2003: Small, highly reflective ice crystals in low-altitude cirrus. *Geophys. Res. Lett.*, **30**, 2132, doi:10.1029/2003GL018153.

Grabowski, W. W., 2001: Coupling cloud processes with the large-scale dynamics using the cloud-resolving convection parameterization (CRCP). *J. Atmos. Sci.*, **58**, 978-997.

Grabowski, W. W., 2003: MJO-like coherent structures: Sensitivity simulations using the cloud-resolving convection parameterization (CRCP). *J. Atmos. Sci.*, **60**, 847-864.

Grabowski, W. W., X. Wu, and M. W. Moncrieff, 1996: Cloud-resolving modeling of tropical cloud systems during phase III of GATE. Part I: Two-dimensional experiments. *J. Atmos. Sci.*, **53**, 3684-3709.

Green, R., and B. A. Wielicki, 1997: Convolution of imager cloud properties with CERES footprint point spread function (Subsystem 4.4). "Clouds and the Earth's Radiant Energy System (CERES) algorithm theoretical basis document, Volumn III: Cloud analyses and radiance inversions (Subsystem 4)", edited by CERES Science Team, December, 1997, 34 pp. [http://asd-www.larc.nasa.gov/ATBD/ATBD.html]

Heymsfield, A. J., D. M. Winker, and G.-J. Zadelhoff, 2005: Extinction-ice water content-effective radius algorithms for CALIPSO. *Geophys. Res. Lett.*, **32**, L10807, doi:10.1029/2005GL022742.

Holz, R. E., S. Ackerman, P. Antonelli, F. Nagle, R. O. Knuteson, M. McGill, D. L. Hlavka, and W. D. Hart, 2006: An improvement to the high spectral resolution CO_2 slicing cloud top altitude retrieval. *J. Atmos. Ocean. Tech*. In press.

IPCC, 2001: Intergovernmental Panel on Climate Change, *Climate Change 2001*, Third Assessment Report of the IPCC. The scientific basis. A contribution of Working Group I. Cambridge University Press.

Jin, Z., T. Charlock, W. Smith, Jr., and K. Rutledge, 2004: A parameterization of ocean surface albedo. *Geophys. Res. Lett.*, **31**, L22301, doi:10.1029/2004GL021180.

Johnson, D. E., W.-K. Tao, J. Simpson, and C.-H. Sui, 2004: A study of the response of deep tropical clouds to large-scale thermodynamic forcings. Part I: Modeling strategies and simulation of TOGA COARE convective systems. *J. Atmos. Sci.*, **59**, 3492-3518.

Johnson R. H., T. M. Rickenbach, S. A. Rutledge, P. E. Ciesielski, and W. H. Schubert, 1999: Trimodal characteristics of tropical convection. *J. Climate*, **12**, 2397-2418.

Khairoutdinov, M. F., and D. A. Randall, 2001: A cloud resolving model as a cloud parameterization in the NCAR Community Climate System Model: Preliminary results. *Geophys. Res. Lett.*, **28**, 3617-3620.

Krueger, S. K., 1988: Numerical simulation of tropical cumulus clouds and their interaction with the subcloud layer. *J. Atmos. Sci.*, **45**, 2221-2250.

Krueger, S. K., G. T. McLean, and Q. Fu, 1995a: Numerical simulation of the stratus-to-cumulus transition in the subtropical marine boundary layer. Part I: Boundary-layer structure. *J. Atmos. Sci.*, **52**, 2839-2850.

Krueger, S. K., G. T. McLean, and Q. Fu, 1995b: Numerical simulation of the stratus-to-cumulus transition in the subtropical marine boundary layer. Part II: Boundary-layer circulation. *J. Atmos. Sci.*, **52**, 2851-2868.

Krueger, S. K., Q. Fu, K. N. Liou, and H-N. S. Chin, 1995: Improvements of an ice-phase microphysics parameterization for use in numerical simulations of tropical convection. *J. Appl. Meteor.*, **34**, 281-287.

Lin, C., 1999a: Some bulk properties of cumulus ensembles simulated by a cloud-resolving model. Part I: Cloud root properties. *J. Atmos. Sci.*, **56**, 3724-3735.

Lin, C., 1999b: Some bulk properties of cumulus ensembles simulated by a cloud-resolving model. Part II: Entrainment profiles. *J. Atmos. Sci.*, **56**, 3736-3748.

Lin, Y.-L., R. D. Farley, and H. D. Orville, 1983: Bulk parameterization of the snow field in a cloud model. *J. Clim. Appl. Meteor.*, **22**, 1065-1092.

Loeb, N. G., N. Manalo-Smith, S. Kato, W. F. Miller, S. K. Gupta, P. Minnis, and B. A. Wielicki, 2003: Angular distribution models for top-of-atmosphere radiative flux estimation from the Clouds and the Earth's Radiant Energy System instrument on the Tropical Rainfall Measuring Mission Satellite. Part I: Methodology. *J. Appl. Meteor.*, **42**, 240-265.

Lord, S. J., H. E. Willoughby, and J. M. Piotrowicz, 1984: Role of a parameterized ice-phase microphysics in an axisymmetric, nonhydrostatic tropical cyclone model. *J. Atmos. Sci.*, **41**, 2836-2848.

Luo, Y., S. K. Krueger, G. G. Mace, and K.-M. Xu, 2003: Cirrus cloud properties from a cloud-resolving model simulation compared to cloud radar observations. *J. Atmos. Sci.*, **60**, 510-525.

Mace, G. G., T. P. Ackerman, P. Minnis, and D. F. Young, 1998: Cirrus layer microphysical properties derived from surface-based millimeter radar and infrared interferometer data. *J. Geophys. Res.*, ***103***, 23,207-23,216.

McClatchey, R. A., R. W. Fenn, J. E. A. Selby, F. E. Volz, and J. S. Garing, 1972: Optical properties of the atmosphere. Environmental Research Paper 411, Air Force Cambridge Research Laboratory, Bedford, Massachusetts, 108 pp. [Available from AFCRL, Bedford, MA 01730.]

Minnis, P., D. F. Young, D. P. Kratz, J. A. Coakley, Jr., M. D. King, D. P. Garber, P. W. Heck, S. Mayor, and R. F. Arduini (1997): Cloud optical property retrieval (Subsystem 4.3). "Clouds and the Earth's Radiant Energy System (CERES) algorithm theoretical basis document. Volumn III: Cloud analyses and radiance inversions (Subsystem 4)", edited by CERES Science Team, December, 1997, 60 pp. [http://asd-www.larc.nasa.gov/ATBD/ATBD.html]

Randall, D. A., and Coauthors, 2003: Confronting models with data. The GEWEX Cloud System Study. *Bull. Amer. Meteor. Soc.*, **84**, 455-469.

Rossow, W. B., L. C. Garder, and A. A. Lacis, 1989: Global seasonal cloud variation from satellite radiance measurements. Part I. Sensitivity of analysis. *J. Climate*, **2**, 419-458.

Stephens, G. L., and Coauthors, 2002: The CloudSat Mission and the A-train. *Bull. Amer. Meteor. Soc.*, **83**, 1771-1790.

Stokes, G. M., and S. E. Schwartz, 1994: The Atmospheric Radiation Measurement (ARM) Program: Programmatic background and design of the Cloud and Radiation Test bed. *Bull. Amer. Meteor. Soc.*, **75**, 1201-1221.

Tao, W.-K., C.-L. Shie, J. Simpson, S. Braun, and P. E. Ciesielki, 2003: Convective systems over the South China Sea: Cloud-resolving model simulations. *J. Atmos. Sci.*, **60**, 2929-2956.

Wang, Z., G. M. Heymsfield, L. Li, and A. J. Heymsfild, 2005: Retrieve optically thick ice cloud microphysical properties by using airborne dual-wavelength radar measurements. *J. Geophys. Res.*, **110**, D19201, doi: 10.1029/2005JD005969.

Wielicki, B. A., B. R. Barkstrom, E. F. Harrison, R. B. Lee III, G. L. Smith, and J. E. Cooper, 1996: Clouds and the Earth's Radiant Energy System (CERES): An Earth Observing System experiment. *Bull. Amer. Meteor. Soc.*, **77**, 853-868.

Wielicki, B. A., B. R. Barkstrom, B. A. Baum, T. P. Charlock, R. N. Green, D. P. Kratz, R. B. Lee, P. Minnis, G. L. Smith, T. Wong, D. F. Young, R. D. Cess, J. A. Coakley, Jr., D. A. H. Crommelynck, L. Donner, R. Kandel, M. D. King, A. J. Miller, V. Ramanathan, D. A. Randall, L. L. Stowe, and R. M. Welch, 1998: Clouds and the Earth's Radiant Energy System (CERES): Algorithm Overview. *IEEE Trans. on Geisha. Re. Sens.*, **36**, 1127-1141.

Winker, D. M., J. Pelon, and M. P. McCormick, 2003: The CALIPSO mission: Spaceborne lidar for observation of aerosols and clouds. *Proc. SPIE*, 4893, pp. 1-11. [Available at http://www-calipso.larc.nasa.gov/resources/more_publications.php]

Xie, S., R. T. Cederwall, M. Zhang, and J. J. Yio, 2003: Comparison of SCM and CSRM forcing data derived from the ECMWF model and from objective analysis at the ARM SGP site. *J. Geophys. Res.*, **108**, 4499, doi:10.1029/2003JD003541.

Xu, K.-M., 2005: The sensitivity of diagnostic radiative properties to cloud microphysics among cloud-resolving model simulations. *J. Atmos. Sci.*, **62**, 1241-1254.

Xu, K.-M., 2006: Using the bootstrap method for a statistical significance test of differences between summary histograms. *Mon. Wea. Rev.*, **134**, 1442-1453.

Xu, K.-M., and S. K. Krueger, 1991: Evaluation of cloudiness parameterizations using a cumulus ensemble model. *Mon. Wea. Rev.*, **119**, 342-367.

Xu, K.-M., and D. A. Randall, 1996: Explicit simulation of cumullus ensembles with the GATE Phase III data: Comparison with observations. *J. Atmos. Sci.*, **53**, 3710-3736.

Xu, K.-M., and D. A. Randall, 2000: Explicit simulation of cumulus ensembles in midlatitude: Comparison with ARM observations. *J. Atmos. Sci.*, **57**, 2839-2858.

Xu, K.-M., and Coauthors, 2002: An intercomparison of cloud-resolving models with the Atmospheric Radiation Measurement summer 1997 Intensive Observation Period data. *Q. J. Roy. Meteor. Soc.*, **128**, 593-624.

Xu, K.-M., T. Wong, B. A. Wielicki, L. Parker, and Z. A. Eitzen, 2005: Statistical analyses of satellite cloud object data from CERES. Part I: Methodology and preliminary results of the 1998 El Niño/2000 La Niña. *J. Climate*, **18**, 2497-2514.

Xu, K.-M., T. Wong, B. A. Wielicki, L. Parker, B. Lin, Z. A. Eitzen, and M. Branson, 2006: Statistical analyses of satellite cloud object data from CERES. Part II: Tropical convective cloud objects during 1998 El Niño and evidence for supporting the fixed anvil temperature hypothesis. Submitted to *J. Climate*.

Figure Captions

Figure1. Vertical profiles of the advective tendencies of (a) potential temperature and (b) water vapor mixing ratio averaged over cloud objects within the four categories: the large-size (L98; solid line), medium-size (M98; long-dashed line), small-size (S98; short-dashed line) cloud objects observed during March 1998 and the large-size cloud objects observed during March 2000 (L00; dots-dashed).

Figure 2. Vertical profiles of the temporally-and-horizontally averaged cloud fraction from the CRM simulations for (a) the large size cloud objects observed during March 1998 (L98; solid line) and March 2000 (L00; dashed line), and (b) the large- (solid line), medium- (long-dashed line), and small-size (short-dashed line) cloud objects observed during March 1998.

Figure 3. Vertical profiles of the temporally-and-horizontally averaged hydrometeor mixing ratios from the CRM simulations for the large size cloud objects observed during the March 1998 (solid line) and March 2000 (dashed line) periods, respectively: (a) Cloud ice, (b) snow, (c) graupel, (d) cloud water, (e) rain, and (f) all hydrometeors.

Figure 4. Summary histograms of cloud top height (upper panels), cloud top temperature (middle panels) and OLR (lower panels) of the large-size cloud objects observed during the March 1998 (L98; left column) and March 2000 (L00; right column) periods: comparisons between the CRM simulations (solid lines) and the CERES observations (dash lines).

Figure 5. Summary histograms of cloud optical depth (upper panels) and TOA albedo (lower panels) of the large-size cloud objects observed during the March 1998 (L98; left column) and March 2000 (L00; right column) periods: comparisons between the CRM simulations (solid lines) and the CERES observations (dash lines).

Figure 6. Same as Fig. 4 except for comparisons of the CERES observations (left column) and the CRM simulations (right column) between the two periods (L98, solid line; L00, dashed line).

Figure 7. Cumulative probability of the CAPE computed using the initial sounding data in the CRM simulations for the large-size (L98; solid line), medium-size (M98; long-dashed line), small-size (S98; short-dashed line) cloud objects observed during the March 1998 period and the large-size cloud object observed during the March 2000 period (L00; dots-dashed line).

Figure 8. Same as Fig. 5 except for comparisons of the CERES observations (left column) and the CRM simulations (right column) between the two periods (L98, solid line; L00, dashed line).

Figure 9. Vertical profiles of the temporally and horizontally averaged hydrometeor mixing ratios from the CRM simulations for the large-size (L98; solid lines), medium-size (M98; long-dashed lines), and small-size (S98; short-dashed lines) cloud objects observed during the March 1998 period: (a) Cloud ice, (b) snow, (c) graupel, (d) cloud water, (e) rain, (f) all hydrometeors.

Figure 10. Summary histograms of cloud top height (a and b), OLR (c and d), albedo (e and f) and cloud optical depth (g and h) of the large-size (L98; solid lines), medium-size (M98; long-

dashed lines), and small-size (S98; dot-dashed line) cloud objects observed during the March 1998 period from the CRM simulations (left column) and the CERES observations (right column).

Figure 11. Comparisons of the summary histograms from the CRM simulations of the large-size cloud objects observed during March 1998 obtained using different analysis methods for (a) cloud top height, (b) OLR, (c) cloud optical depth, and (d) albedo: RMA, COL, and EX. See the text for detailed explanations of RMA, COL, and EX methods.

Figure 12. D_{ge} determined by three different formulations: (a) $D_{ge}(IWC)$, (b) $D_{ge}(IWC, T)$, and (c) $D_{ge}(T)$. See Eqs. (1), (2) and (3) in the text for the formulations.

Figure 13. Comparisons of the summary histograms from the CRM simulations of the large-size cloud objects observed during March 1998 obtained using different formulae of D_{ge} for (a) cloud top height, (b) OLR, (c) cloud optical depth, and (d) TOA albedo: short-dashed line represents $D_{ge}(IWC)$, long-dashed line $D_{ge}(T)$, dots-dashed line $D_{ge}(IWC, T)$, and the CERES observations (solid line).

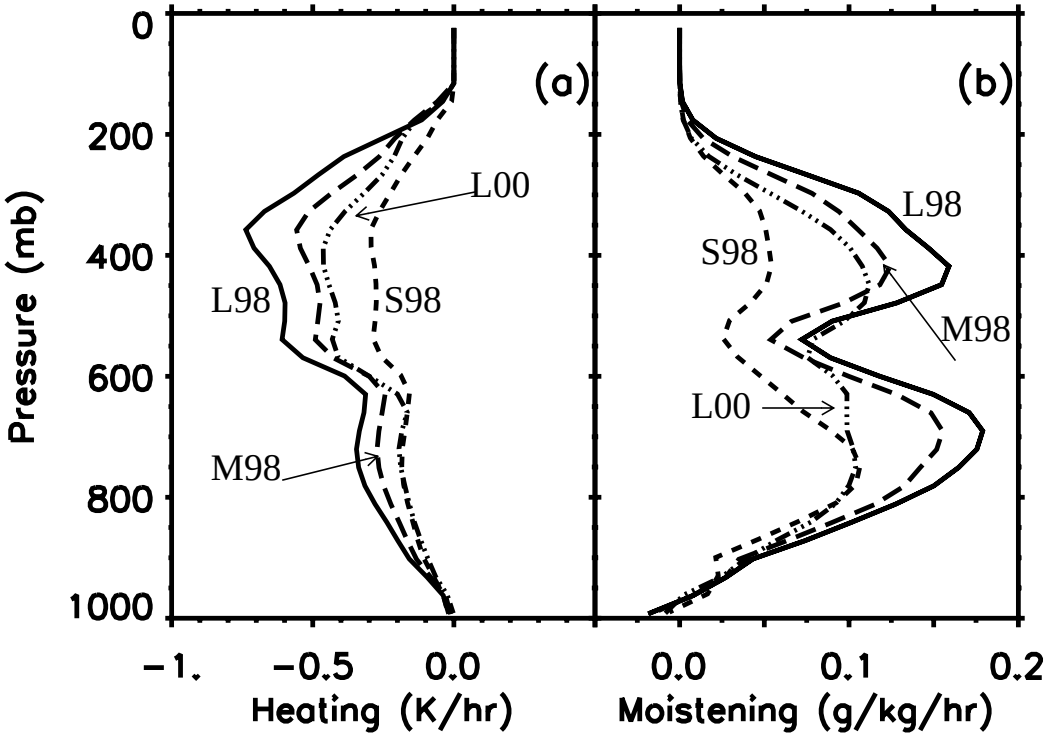

Figure 1. Vertical profiles of the advective tendencies of (a) potential temperature and (b) water vapor mixing ratio averaged over cloud objects within the four categories, respectively: the large-size (L98; solid line), medium-size (M98; long-dashed line), small-size (S98; short-dashed line) cloud objects observed during March 1998, and large-size cloud objects observed during March 2000 (L00; dot-dashed line).

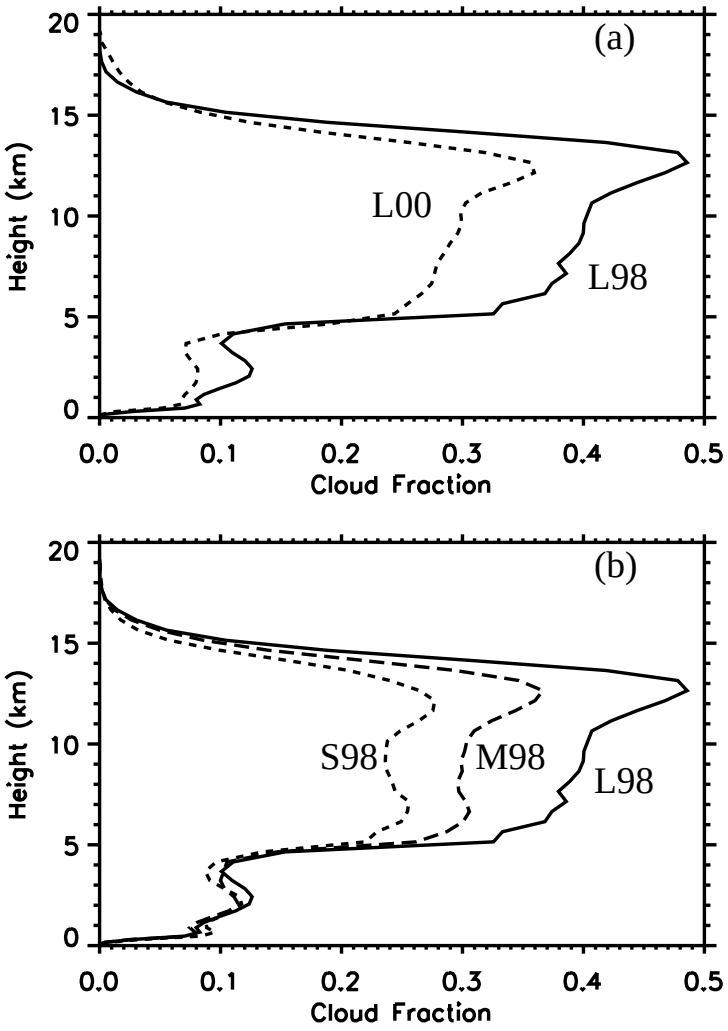

Figure 2. Vertical profiles of the temporally and horizontally averaged cloud fraction from the CRM simulations. The upper panel represents the large-size cloud objects observed during March 1998 (L98; solid line) and March 2000 (L00; dashed line) periods. The lower panel represents the large-size (L98; solid line), medium-size (M98; long-dashed line), and small-size (S98; short-dashed line) cloud objects observed during the March 1998 period.

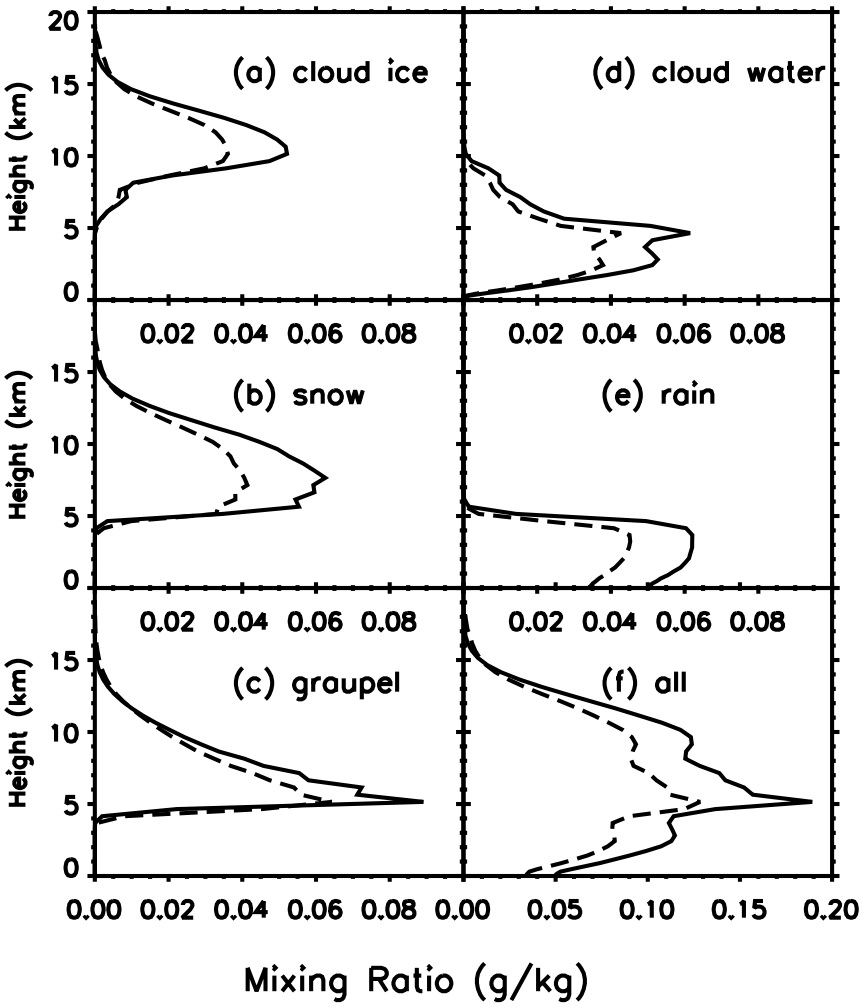

Figure 3. Vertical profiles of the temporally and horizontally averaged mixing ratios of hydrometeors from the CRM simulations for the large-size cloud objects observed during March 1998 (solid line) and March 2000 (dashed line) periods, respectively: (a) cloud ice, (b) snow, (c) graupel, (d) cloud waterc (e) rain, (f) all hydrometeors.

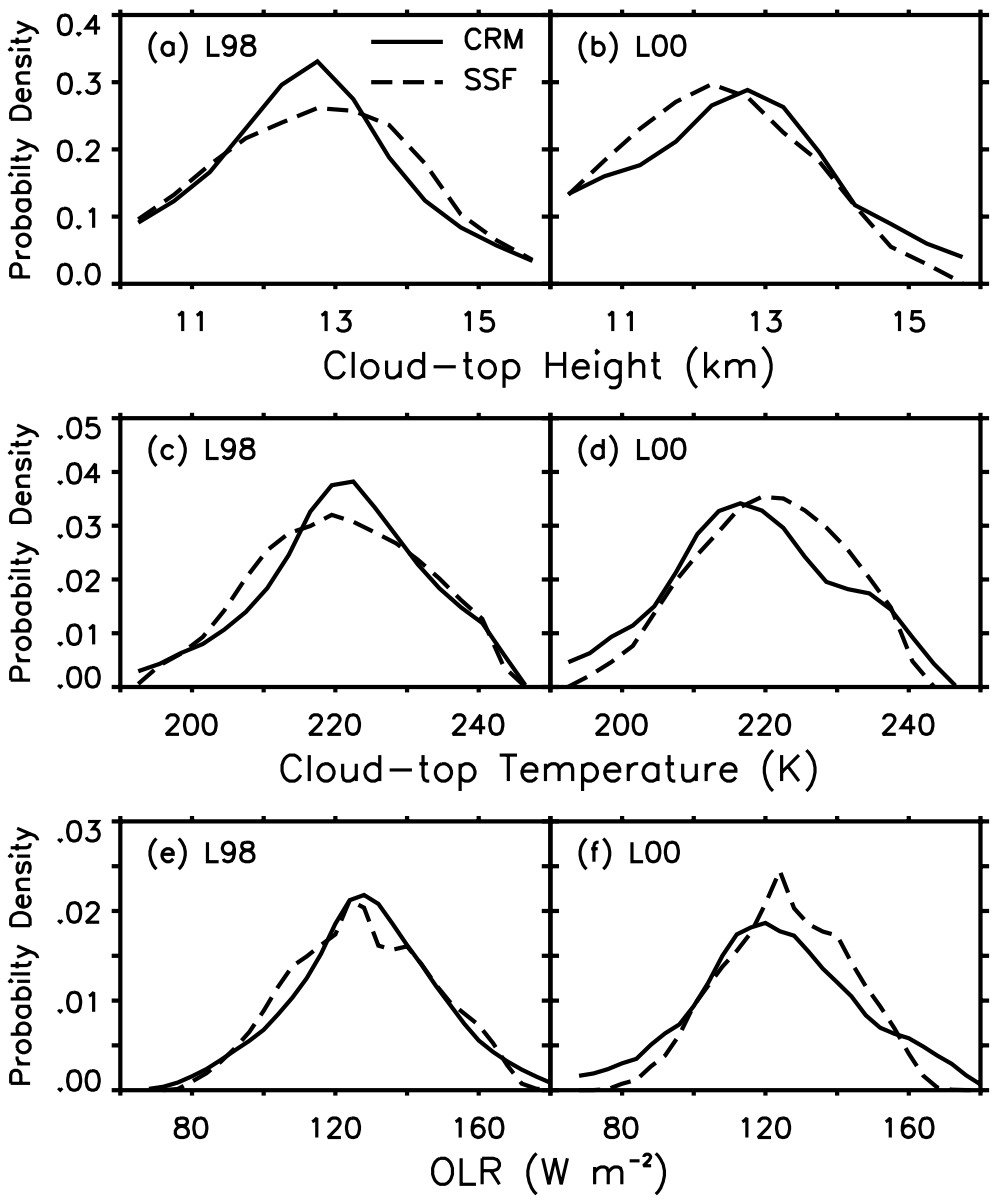

Figure 4. Summary histograms of cloud top height (upper panels), cloud top temperature (middle panels) and OLR (lower panels) of the large-size cloud objects observed during the March 1998 (L98; left column) and March 2000 (L00; right column) periods: comparisons between the CRM simulations (solid lines) and the CERES observations (dashed lines).

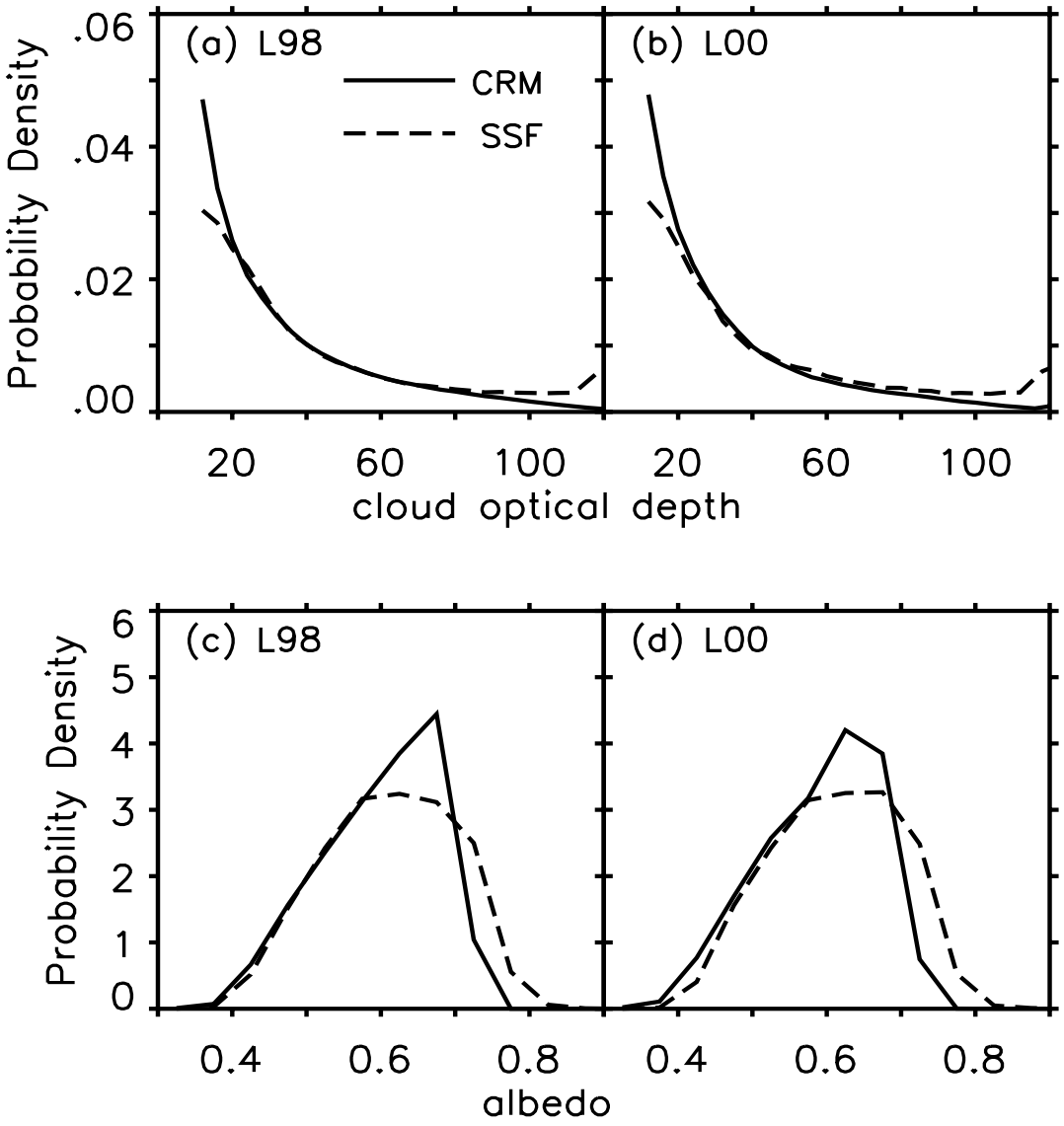

Figure 5. Summary histograms of cloud optical depth (upper panels) and TOA albedo (lower panels) of the large-size cloud objects observed during the March 1998 (L98; ;eft column) and March 2000 (L00; right column) periods: comparisons between the CRM simulations (solid lines) and the CERES observations (dashed lines).

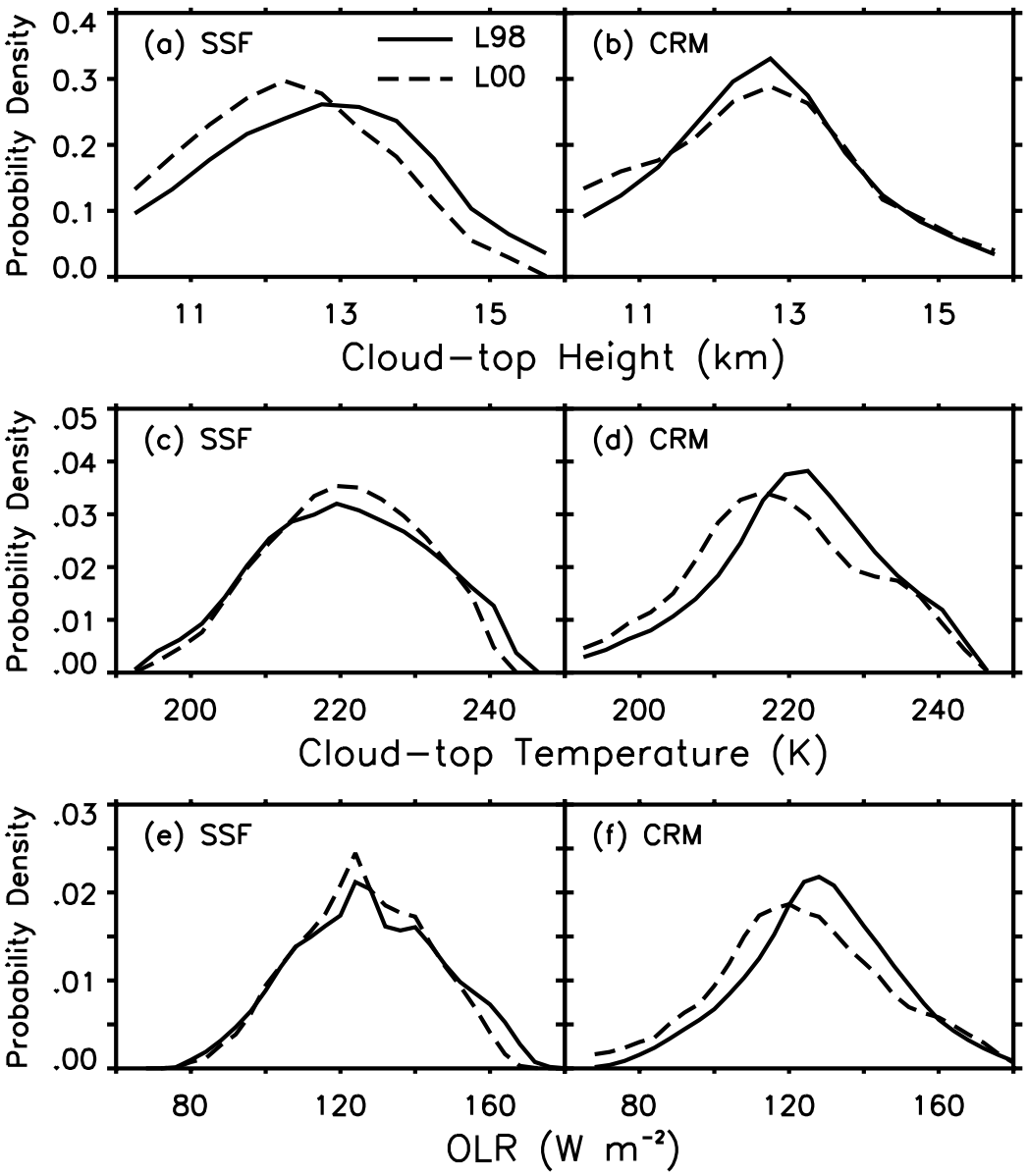

Figure 6. Same as Fig. 4 except for comparisons of the CERES observations (left column) and the CRM simulations (right column) between the two periods (L98, solid lines; L00, dashed lines).

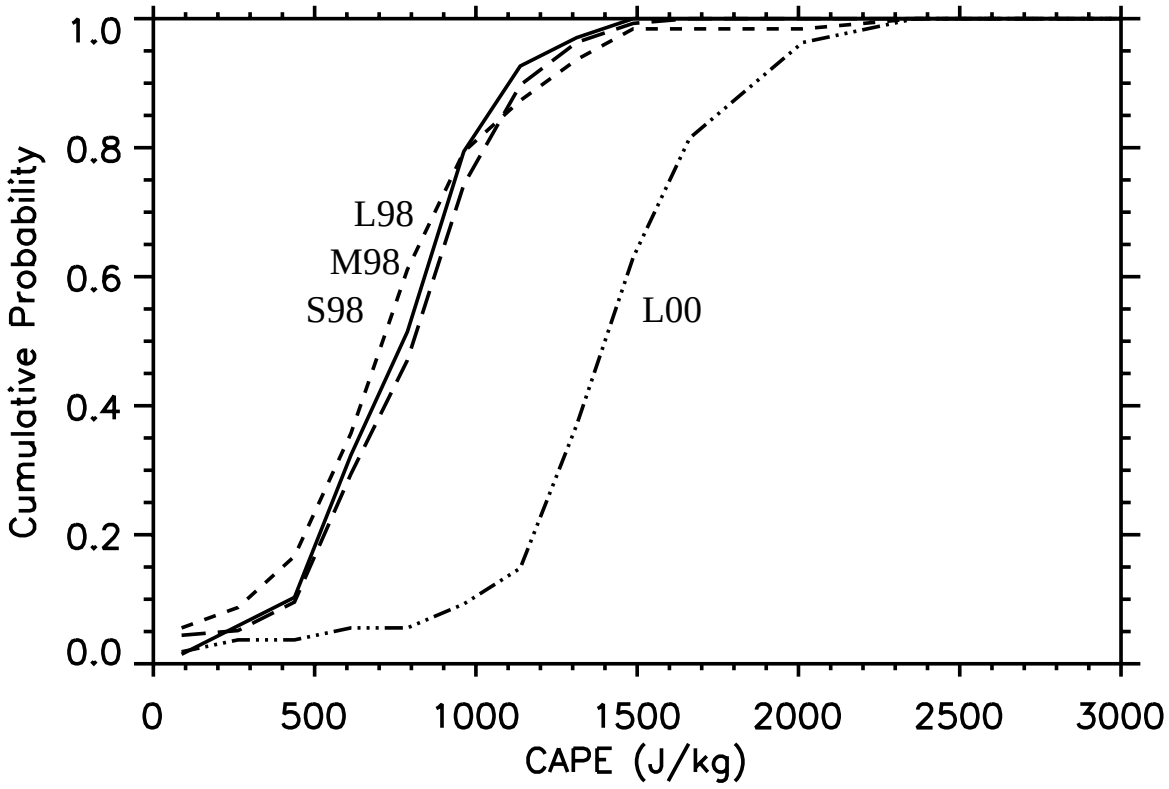

Figure 7. Cumulative probability of the CAPE computed using the initial soundings in the CRM simulations for the large-size (L98; solid line), medium-size (M98; long-dashed line), small-size (S98; short-dashed line) cloud objects observed during the March 1998 period and the large-size cloud objects observed during the March 2000 period (L00; dot-dashed line).

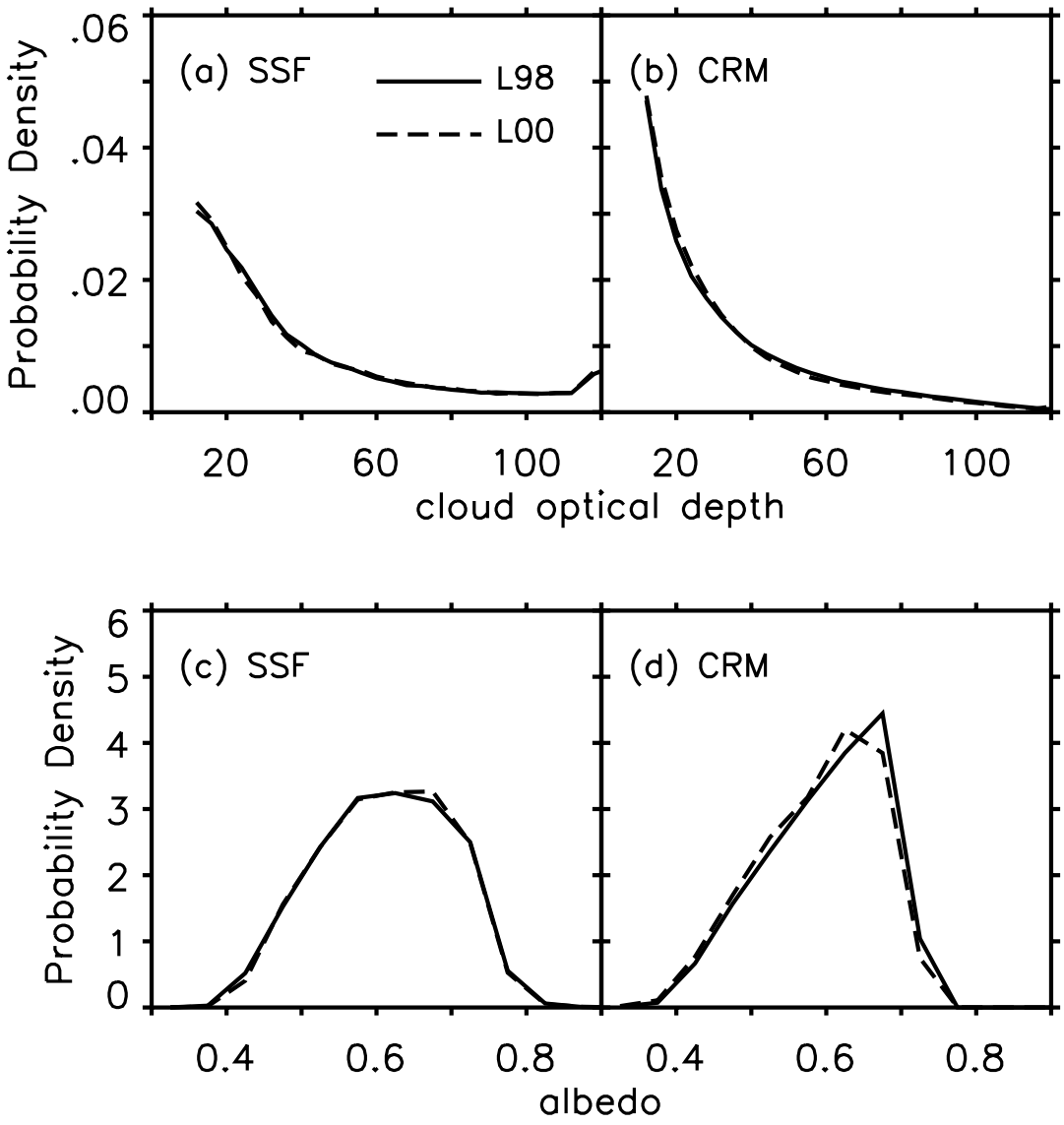

Figure 8. Same as Fig. 5 except for comparisons of the CERES observations (left column) and the CRM simulations (right column) between the two periods (L98, solid lines; L00, dashed lines).

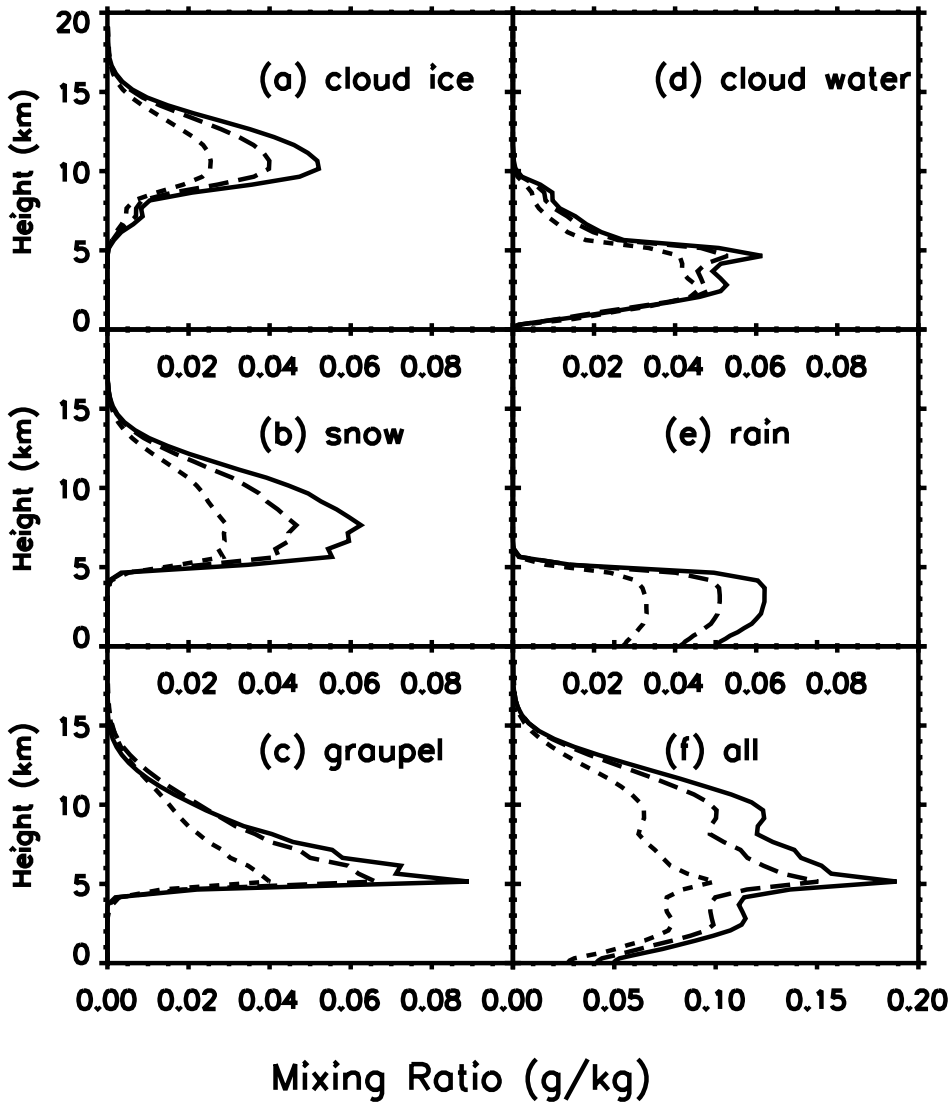

Figure 9. Vertical profiles of the temporally and horizontally averaged mixing ratios of hydrometeors from the CRM simulations for the large-size (solid lines), medium-size (long-dashed lines), and small-size (short-dashed lines) cloud objects observed during the March 1998 period. (a) Cloud ice. (b) Snow. (c) Graupel. (d) Cloud water. (e) Rain. (f) All hydrometeors.

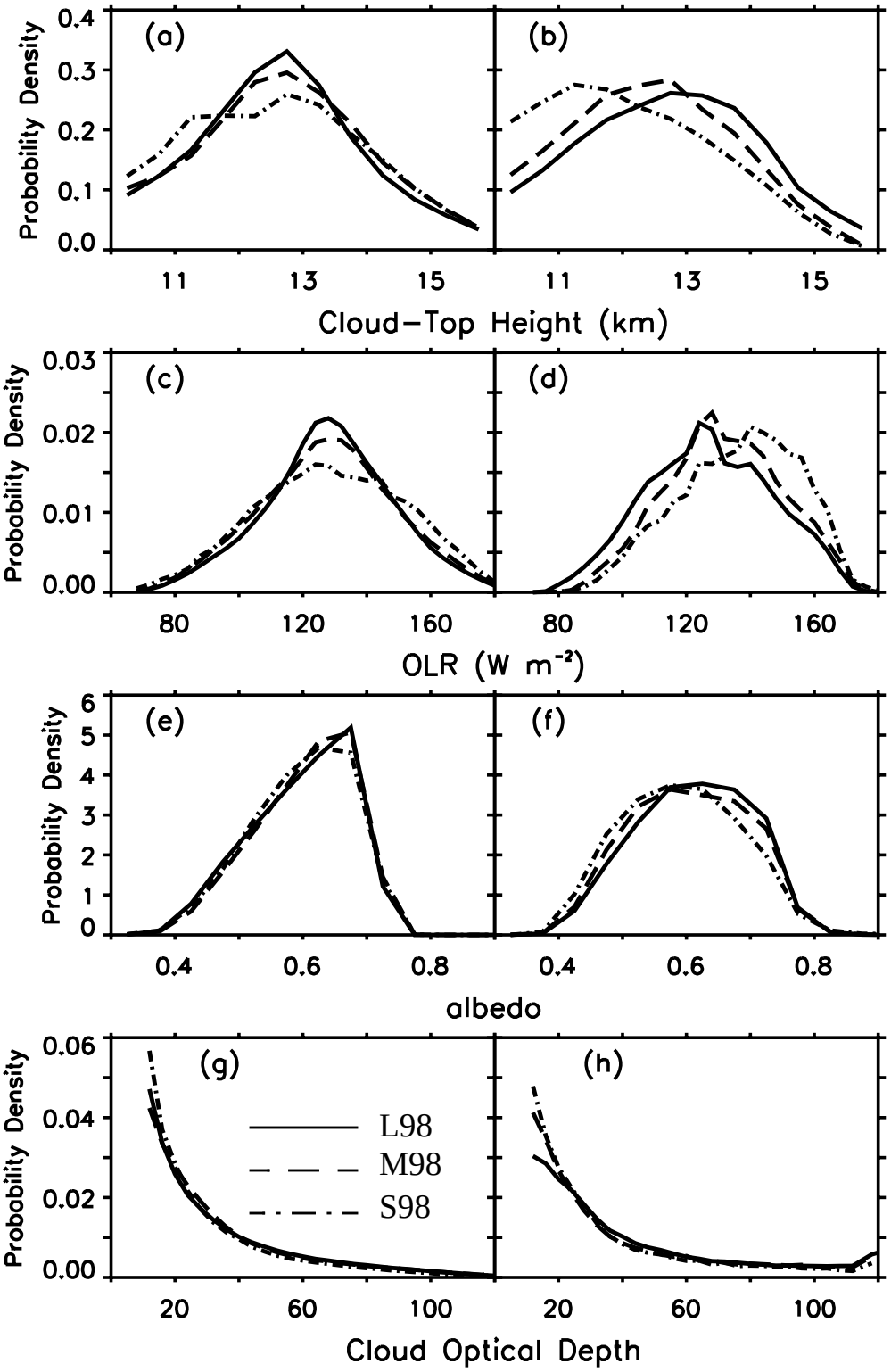

Figure 10. Summary histograms of cloud top height (a and b), OLR (c and d), TOA albedo (e and f) and cloud optical depth (g and h) of the large-size (L98; solid lines), medium-size (M98; long-dashed lines), and small-size (S98; dot-dashed lines) cloud objects observed during the March 1998 period from the CRM simulations (left column) and the CERES observations (right column).

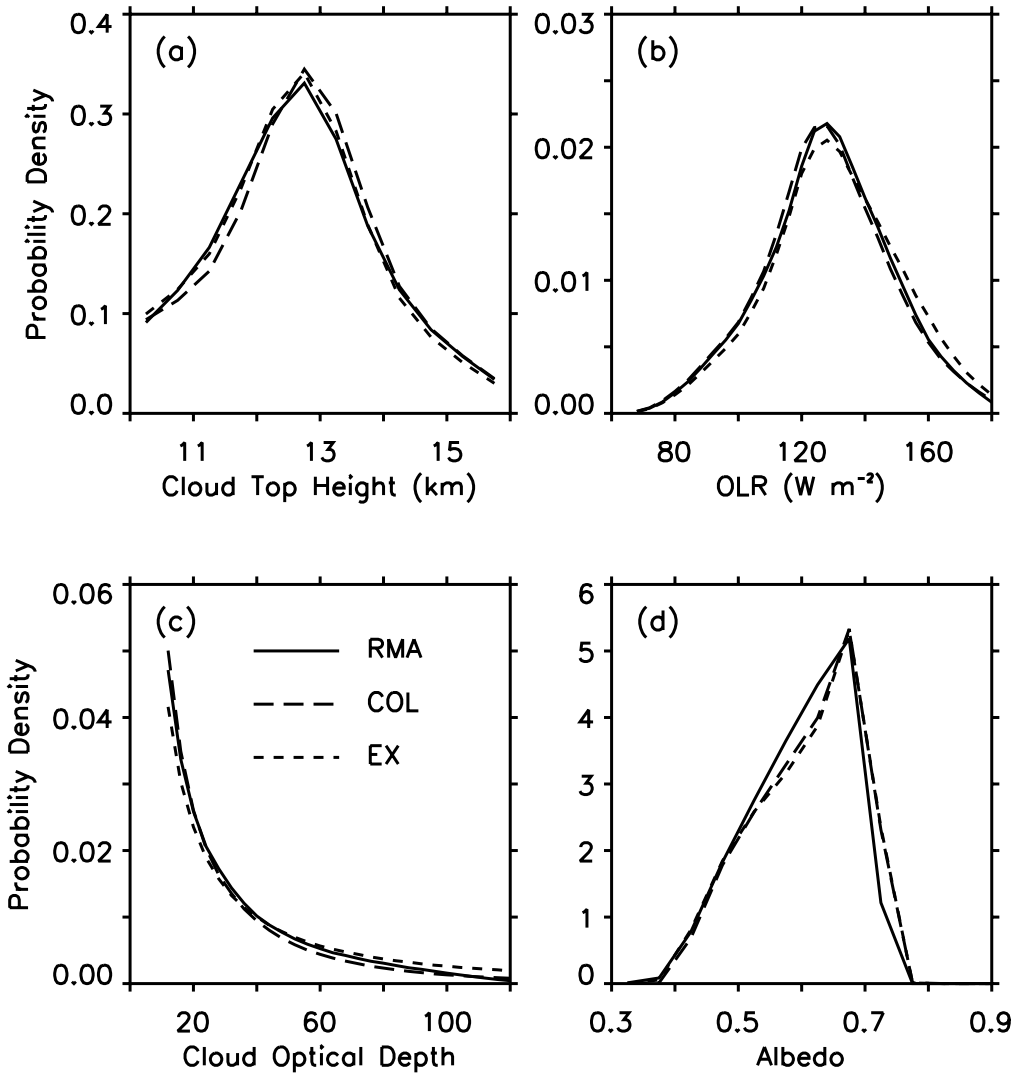

Fig11. Comparisons of the summary histograms from the CRM simulations for the large-size cloud objects observed during March 1998 obtained using different analysis methods for (a) cloud top height, (b) OLR, (c) cloud optical depth, (d) albedo: RMA (solid line), COL (long-dashed line), and EX (short-dashed line). See the text for detailed explanation of RMA, COL, and EX.

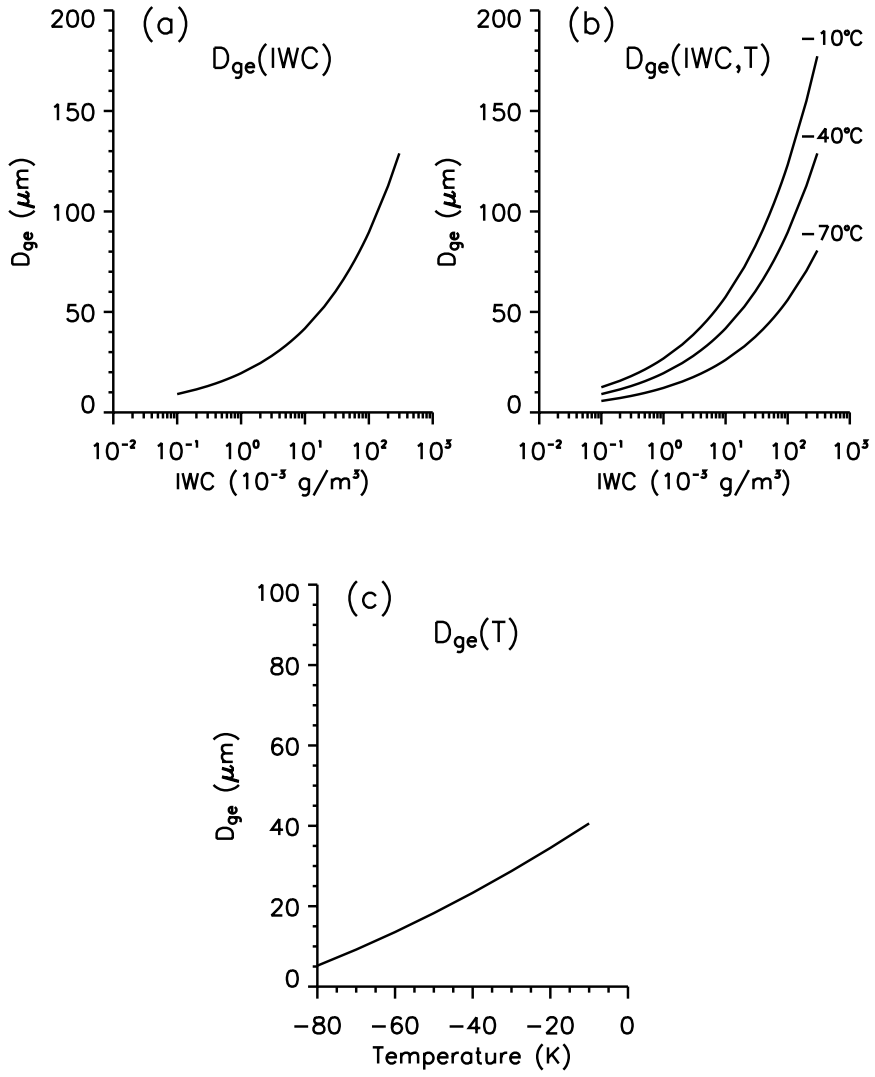

Figure 12. Dge determined by the three different formulations: (a) Dge (IWC), (b) Dge (IWC,T), and (c) Dge (T). Please see the equations 1, 2, and 3 in the text for the formulations.

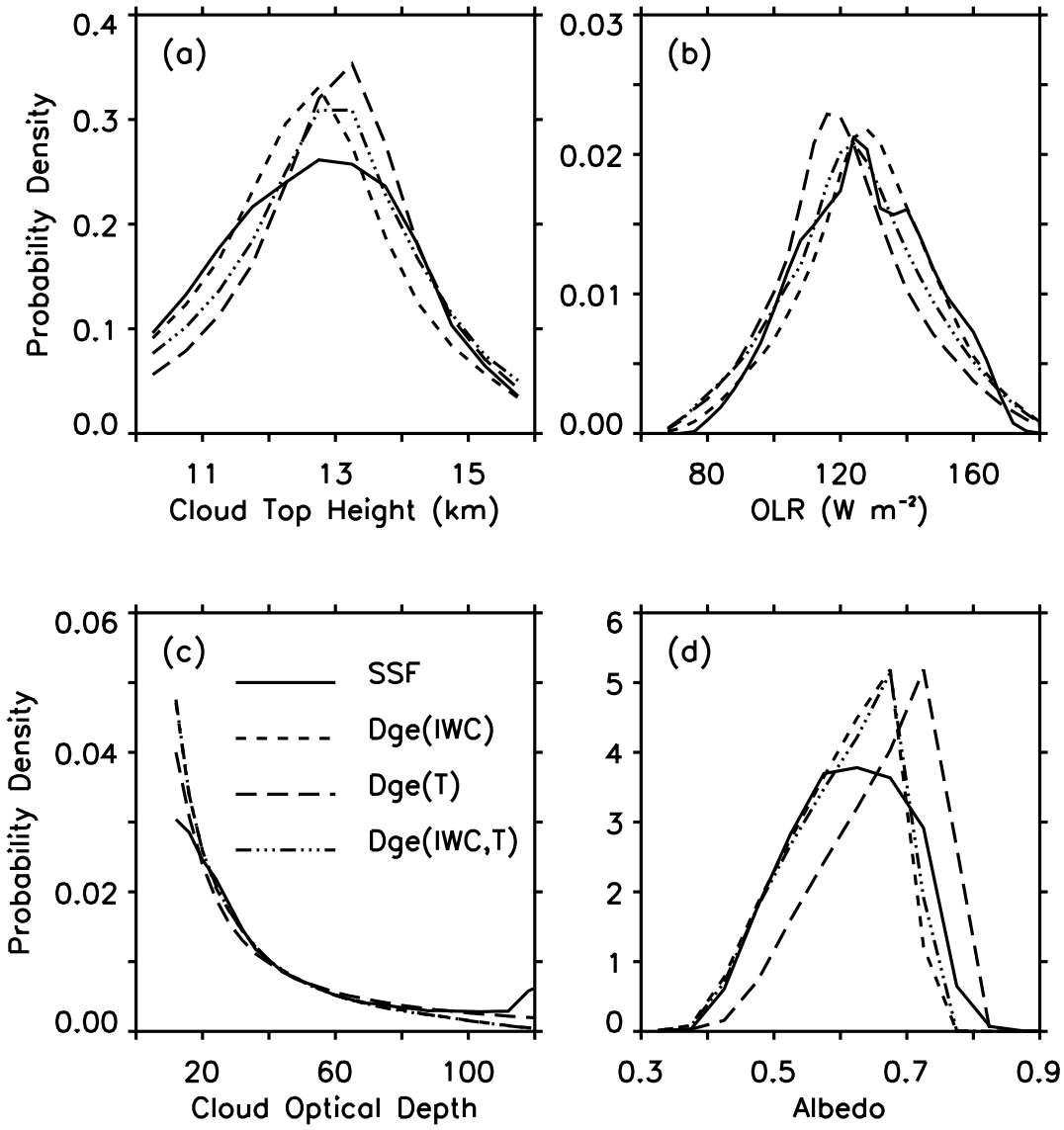

Fig13. Comparisons of the summary histograms for the large-size cloud objects observed during March 1998 from three sets of CRM simulations obtained using different formulae of Dge for (a) cloud top height, (b) OLR, (c) cloud optical depth, (d) albedo: short-dashed line represents Dge (IWC), long-dashed line Dge (T), dots-dashed line Dge (IWC,T), and the CERES observations (solid line). See the text for detailed explanation of Dge(IWC), Dge(T), and Dge(IWC,T).

TABLE 1. Summary of the four ensembles of simulations performed in this study.

Category	Period of cloud objects	Equivalent diameter of cloud objects	Number of cloud objects	CRM's domain width (km)	CRM's Δx (km)
L98	March 1998	> 300 km	68	1024	2
M98	March 1998	150 - 300 km	136	512	2
S98	March 1998	100 - 150 km	126	256	2
L00	March 2000	> 300 km	54	512	2

TABLE 2. Measured L2 distances and p values (%) for the two ensembles of large-size cloud objects observed during March 1998 and March 2000, respectively. “CM98” and “CM00” represent results from the CRM simulations. “O98” and “O00” represent the CERES cloud object data.

parameter	CM98 vs. O98		CM00 vs. O00		O98 vs. O00		CM98 vs. CM00	
	L2	p	L2	p	L2	p	L2	p
OLR	0.036	7.6	0.060	2.9	0.034	7.9	0.061	3.6
albedo	0.125	< 0.1	0.127	< 0.1	0.011	95.9	0.047	19.4
cloud top height	0.060	1.6	0.058	14.4	0.081	0.1	0.041	43.6
cloud top temperature	0.048	1.8	0.062	4.6	0.038	7.9	0.071	2.0
cloud optical depth	0.066	< 0.1	0.065	< 0.1	0.011	77.0	0.015	52.2

TABLE 3. Measured L2 distances between the CRM simulations and the CERES cloud object data and the p values (%) for the large-size (L98), medium-size (M98), and small-size (S98) cloud objects observed during March 1998.

parameter	L98		M98		S98	
	L2	p	L2	p	L2	p
OLR	0.036	7.6	0.043	0.8	0.080	0.1
albedo	0.125	< 0.1	0.136	< 0.1	0.118	< 0.1
cloud top height	0.060	1.6	0.051	2.1	0.091	0.5
cloud top temperature	0.048	1.8	0.049	0.7	0.087	0.2
cloud optical depth	0.066	< 0.1	0.024	12.4	0.037	12.3

TABLE 4. Measured L2 distances between the large-size and medium-size, the medium-size and small-size, and the small-size and large-size cloud objects of March 1998, respectively, and the p values (%) as revealed by the CERES cloud object data.

parameter	L2 distance			p value (%)		
	L and M	M and S	L and S	L and M	M and S	L and S
OLR	0.044	0.066	0.093	0.9	< 0.1	< 0.1
albedo	0.036	0.050	0.079	20.7	6.1	0.1
cloud top height	0.057	0.086	0.125	1.5	< 0.1	< 0.1
cloud top temperature	0.048	0.072	0.103	1.2	< 0.1	< 0.1
cloud optical depth	0.050	0.029	0.075	0.3	16.8	< 0.1

TABLE 5. Measured L2 distances between the CRM-simulated large-size and medium-size, the medium-size and small-size, and the small-size and large-size cloud objects of March 1998, respectively, and the p values (%).

parameter	L2 distance			p value (%)		
	L and M	M and S	L and S	L and M	M and S	L and S
OLR	0.022	0.036	0.055	49.3	21.1	3.9
albedo	0.028	0.034	0.040	43.4	37.7	29.9
cloud top height	0.029	0.053	0.067	45.9	13.6	5.6
cloud top temperature	0.023	0.041	0.053	53.6	18.6	8.3
cloud optical depth	0.024	0.061	0.044	13.9	0.2	3.8

TABLE 6. Measured L2 distances between the CERES cloud object data and the CRM results and the p values (%) for the large-size cloud objects observed during the March 1998 period. COL: the CRM results without averaging. EX: the CRM results analyzed using the same method as in Eitzen and Xu (2005). EX05: the results from Eitzen and Xu (2005). See the text for more detailed explanations for COL and EX.

parameter	L2 distance			p value (%)		
	COL	EX	EX05	COL	EX	EX05
OLR	0.034	0.039	0.092	7.6	2.7	1.2
albedo	0.099	0.099	0.145	< 0.1	< 0.1	< 0.1
cloud top height	0.065	0.069	0.163	0.8	0.4	< 0.1
cloud top temperature	0.055	0.057	0.127	0.6	0.4	0.1
cloud optical depth	0.081	0.059	0.077	< 0.1	< 0.1	< 0.1